Journal of Colloid and Interface Science 646 (2023) 633–648

Contents lists available at ScienceDirect

Journal of Colloid And Interface Science

journal homepage: www.elsevier.com/locate/jcis

High-performance photocatalytic peroxymonosulfate activation by carbon quantum dots via precise surface chemistry regulation: Insight into the structure–function relations

Wenyuan Han [a,1], Degang Li [b,1], Yifan Kong [b], Wei Liu [c], Wenwu Qin [a,e,*], Shaobin Wang [d], Xiaoguang Duan [d,*]

[a] Key Laboratory of Nonferrous Metal Chemistry and Resources Utilization of Gansu Province, State Key Laboratory of Applied Organic Chemistry and Key Laboratory of Special Function Materials and Structure Design (MOE), College of Chemistry and Chemical Engineering, Lanzhou University, Lanzhou 730000, PR China
[b] School of Chemistry and Chemical Engineering, Shandong University of Technology, Zibo 255000, PR China
[c] School of Chemistry and Environmental Engineering, Sichuan University of Science and Engineering, ZiGong 643000, PR China
[d] School of Chemical Engineering, The University of Adelaide, Adelaide, SA 5005, Australia
[e] Academy of Plateau Science and Sustainability, People's Government Of Qinghai Province & Beijing Normal University, Xining, 810016, China

GRAPHICAL ABSTRACT

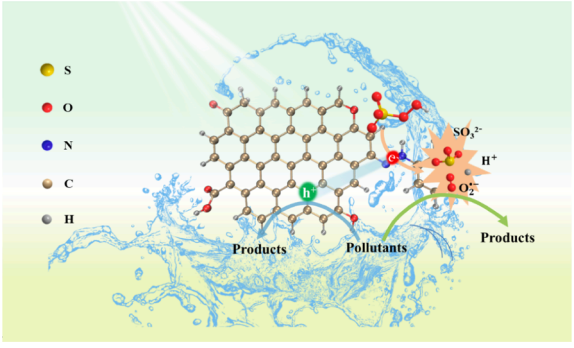

ARTICLE INFO

Keywords:
Carbon quantum dots (CQDs)
Carbonyl group
Photocatalytic
Peroxymonosulfate
Electronic structure
DFT

ABSTRACT

Carbon quantum dots (CQDs) are considered promising metal-free green catalysts for the activation of persulfates, but direct experimental evidence to identify the true active sites on the surface of CQDs is still lacking. We prepared CQDs with different oxygen contents by controlling the carbonisation temperature, using a simple pyrolysis method. Photocatalytic activity experiments show that $CQDs_{200}$ exhibits the best PMS activation performance. By investigating the relationship between the oxygen functional groups on CQDs surface and photocatalytic activity, it was postulated that the C=O groups might be the predominant active site, which was confirmed by selective chemical titrations of the C=O, C-OH and COOH groups. Furthermore, limited to the weak photocatalytic properties of the pristine CQDs, ammonia and phenylhydrazine were used to precisely nitrogen-modify the o-CQD surface. We found that phenylhydrazine-modified o-CQDs-PH promoted the absorption of

* Corresponding authors.
E-mail addresses: qinww@lzu.edu.cn (W. Qin), xiaoguang.duan@adelaide.edu.au (X. Duan).
[1] These authors have contributed equally to this work.

https://doi.org/10.1016/j.jcis.2023.05.092
Received 22 April 2023; Received in revised form 3 May 2023; Accepted 14 May 2023
Available online 18 May 2023

visible light and the separation of photocarriers, thus enhancing the activation of PMS. Theoretical calculations provide more insights from different levels of the pollutant, fine-tuned CQDs, and their interactions.

1. Introduction

With the development of modern society, there has been soaring press on environmental issues. Nanotechnology is one of the solutions for environmental protection, and global efforts are being made to reduce environmental pollution and protect human health[1,2]. Carbon-based nanomaterials, including carbon nanotubes, carbon nanosheets, nanodiamonds, graphene, carbon quantum dots (CQDs), as well as fullerene, have unique properties, such as high specific surface area, large pore volume, and excellent aqueous stability. Therefore, they have been widely used for diverse environmental applications such as membrane-based separations, energy conversion and storage, adsorption and catalytic degradation for contaminant removal[3,4]. Although conventional semiconductor quantum dots (SQDs) offer several advantages, such as high quantum yields, photostability and size-dependent emission wavelengths, there are concerns about the environmental hazards of most SQDs due to their potential toxicity and leaching of metal ions. In contrast to SQDs, low-cost CQDs have favorable physiochemical features without the concern of inherent toxicity or elemental shortage. Therefore, CQDs have been extensively applied in bioimaging, catalysis, sensors, and photovoltaic devices[5–8].

In the past decade, great efforts have been made to develop facile and low-cost methods for CQDs production, which can be divided into top-down and bottom-up approaches[9,10]. The top-down methods via downsizing bulk or nanomaterials into quantum dots suffer from several disadvantages, such as harsh reaction conditions, the requirement of special equipment, low yield, and non-selectivity in size (chemical cutting process). Because the top-down methods typically does not allow for presice control over the size distribution of the products. Therefore, “bottom-up” approachs can realize the synthesis of CQDs with specific molecular size, composition and shape, thus realizing manipulated properties for catalysis[11,12].

Although the photoluminescence (PL) mechanism of CQDs is still controversial, researchers have come to the general conclusion that CQDs could be considered as semiconductors that could generate electrons and holes under light excitation[13]. Due to the large specific surface area and surface-to-volume ratio of carbon dots, a great proportion of carbon atoms are exposed on the surface, resulting in a large amounts of dangling bonds with unpaired electrons that would interact to form an electronic state[14]. Thus, the surface electronic state significantly affects its physical properties, such as energy band structure, free carrier density and local conductivity[15,16]. Unfortunately, pristine CQDs alone has poor photocatalytic degradation activity because of weak light absorption and difficult carrier separation[17]. To regulate the electronic properties and photocatalytic activity, CQDs have been loaded on other semiconducting materials, such as C_3N_4, Ag_3PO_4 and TiO_2, to form nanocomposites[18–21]. However, several factors severely hinder their practical applications, including limited light absorption, additional surface doping, and cumbersome separation [22]. To efficiently utilize energy obtained from sunlight and facilitate the photochemical reaction, the surface states can be manipulated to improve the utilization of excitation energy in CQDs. This would allow the development of surface groups or surface compositions of CQDs that can direct, classify and respond to excitation energy[23,24].

In this article, we report a simple pyrolysis method to produce CQDs from maltitol and hydrogen peroxide. CQDs with different oxygen contents was controlled carbonization temperature. CQDs are further applied to activate PMS to evolve reactive oxygen species (ROS) and degrade antibiotic contaminants, where $CQDs_{200}$ demonstrated the best PMS activation performance attaining 51.5% TC removal in 60 min. Benzoic anhydride (BA), 2-bromo-1-phenylethanone (BrPE), sodium borohydride ($NaBH_4$) and Diss-Martin Periodinane (DMP) were used to specifically titrate oxygen functional groups on the $CQDs_{200}$ surface. The titration experiments were used to elucidate the active contribution of different oxygen functional groups to PMS activation, and ketonic groups (C═O) are identified as the most active sites. Furthermore, limited to the weak photocatalytic properties of pristine CQDs (the highest TC removal 67.4% for o-CQDs), we used phenylhydrazine and ammonia as nitrogen sources to modify the surface chemistry of o-CQDs. It was found that the functionalization of amino groups (–NH_2) to the surface of o-CQDs via ammonia treatment led to promoted radiation recombination of electrons and holes on the surface of o-CQDs, which was not conducive to activating PMS. The phenylhydrazine modification of o-CQDs (o-CQDs-PH) promotes the absorption of visible light and the effective separation of photocarriers, thereby enhancing PMS activation to improve photocatalytic activity in generating ROS and degrading diverse antibiotic contaminants. Meanwhile, theoretical calculations further validated the experimental results of photocatalytic activity.

2. Materials and methods

2.1. Chemicals

Maltitol, peroxymonosulfate (PMS, 42%~46% $KHSO_5$ basis), sodium hydroxide (NaOH, 98%) and methanol (MA, 99%) were purchased from McLean Reagent Co., Ltd (Shanghai, China). Hydrogen peroxide (H_2O_2, 30 wt%) aqueous solution, sulfuric acid (H_2SO_4), Sodium borohydride ($NaBH_4$, 98%), dichloromethane ($CHCl_2$) and ammonium oxalate (AMO, 99%) were purchased from Sinopharm Chemical Reagent Co., Ltd (Shanghai, China). Graphite phase carbon nitride (g-C_3N_4), reduced graphene oxide (rGO) and multi-walled carbon nanotubes (MWCNTs) were purchased from XFNANO Materials Tech. Co Ltd (Nanjing, China). Tetracycline hydrochloride (TC, 96%), doxycycline (DC, 98%), Oxytetracycline (OC, 95%), benzoic anhydride (BA, 98 %), 2-bromo-1-phenylethanone(BrPE, 98 %), 1,1,1-Triacetoxy-1,1-Dihydro-1,2-Benziodoxol-3(1H)-One(DMP, 98%), phenylhydrazine (PH, 99%), Ammonia (NH_4OH), *tert*-butanol (TBA, 99%), p-benzoquinone (BQ, 99%) silver nitrate (SN, 99 %) were purchased from Adamas Reagent Co., Ltd (Shanghai, China). All chemical reagents were used without further purification.

2.2. Preparation of CQDs and CQDs-derivatives

A one-step pyrolysis method was used to prepare CQDs from maltitol and hydrogen peroxide (see **Text S1** for synthesis details). In order to adjust the composition of oxygen functional groups in the CQDs, the carbonisation process was carried out at different temperatures of 180 °C, 200 °C, 220 °C and 240 °C, denoted as $CQDs_{180}$, $CQDs_{200}$, $CQDs_{220}$ and $CQDs_{240}$, respectively.

To selectively block specific functional groups on the surface of $CQDs_{200}$, BA, BrPE, $NaBH_4$, DMP, NH_4OH and PH were chosen for the chemical titration on the surface of CQDs. The modification process is described in detail in **Text S1**. The CQDs-derivatives prepared from BA, BrPE, $NaBH_4$, DMP, NH_4OH and PH are referred to as CQDs-BA, CQDs-Br, r-CQDs, o-CQDs, o-CQDs-NH and o-CQDs-PH, respectively.

2.3. Characterization

Transmission electron micrographs (TEM) and high-resolution TEM (HRTEM) were obtained on a FEI Tecnai G2 F20 TEM (US) operating at 200 kV. X-ray diffraction (XRD) patterns were tested on a Brucker D8 Advance diffractometer with Cu Kα radiation (Germany). Raman spectra

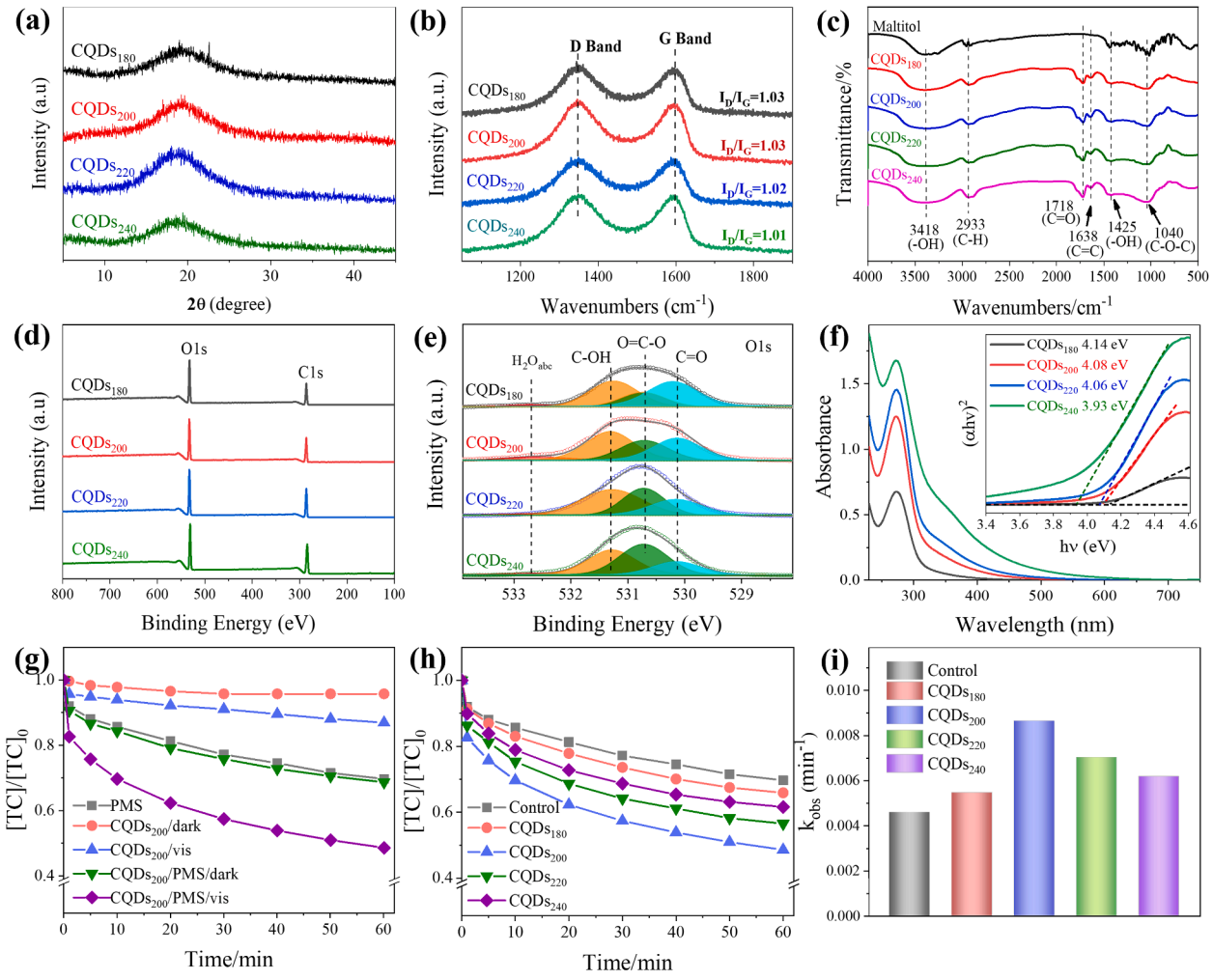

Fig. 1. (a) XRD patterns, (b) Raman spectra, (c) FT-IR spectra, (d) XPS survey scans, (e) O1s XPS spectra and (f) UV–vis absorption spectra of $CQDs_{180}$, $CQDs_{200}$, $CQDs_{220}$ and $CQDs_{240}$. (g) Time-dependent degradation of TC by PMS in the absence and presence of $CQDs_{200}$. (h) Comparison of the performance of $CQDs_{180}$, $CQDs_{200}$, $CQDs_{220}$ and $CQDs_{240}$ in PMS activation under visible lights and (b) the corresponding pseudo-first order kinetic constants (k_{obs}). ($[TC]_0$ = 10 mg/L; [Catalysts] = 0.5 g/L; $[PMS]_0$ = 0.0246 g/L = 0.4 mM; T = 25 °C).

were recorded using a LabRAM HR800 spectrometer (France). Fourier-transform infrared (FT-IR) spectra were obtained on a Nicolet 5700 spectrometer (US) using the KBr pellet technique. X-ray photoelectron spectroscopy (XPS) data were measured on a Kratos Axis UltraDLD spectrometer using a monochromatic Al Kα radiation. The UV–Vis absorption spectra were recorded on a Shimadzu UV-2450PC spectrophotometer (Japan). The PL spectra were obtained from a Hitachi F-4600 luminescence spectrometer (Japan). Electron spin resonance (ESR) signals were recorded on a Bruker A300 spectrometer (USA) at room temperature. Electrochemical tests were performed on an electrochemical workstation CHI660D (China). The as-prepared CQDs and modified CQDs were used as the working electrode separately. The platinum wire and saturated calomel electrode (SCE) were used as counter electrod and reference electrode, respectively. The electrolyte was 0.05 M Na_2SO_4 solution. The working electrode was irradiated with visible light obtained from a BoPhilae PLS-SXE300DUV 300 W Xelamp (Beijing) with a 420 nm cut-off filter. Chopped-light amperometric I-t characterizations were evaluated under visible light irradiation. Electrochemical impedance spectroscopy (EIS) was conducted at frequencies ranging from 0.1 Hz to 100 kHz and 5 mV.

2.4. Photocatalytic activities test

The photocatalytic experiment was evaluated by using a 300 W Xe lamp with a 420 nm cut-off filter. Before the irradiation and the addition of PMS, a certain amount of photocatalyst was dispersed in 100 mL TC aqueous solution with magnetic stirring for 30 min in dark to establish the absorption–desorption equilibrium. The distance between the light source and the liquid surface was 10 cm. Then, PMS was quickly added to the solution to initiate the photocatalytic experiment after turning on the light. The initial pH of the reaction solution was adjusted by using 0.1 M H_2SO_4 and 0.1 M NaOH. At designated time intervals, 3 mL samples were taken and mixed with sodium sulfite ($NaSO_3$) to quench the reaction. The concentration of TC, DC and OC were analyzed using a high performance liquid chromatography (HPLC, Thermo-Fisher, USA) equipped with a SB-C18 (Agilent Poroshell 120) column (see Table S1 for details). The residual PMS concentration in the solution was determined by colorimetric method, and the details were presented in **Text S2**.

2.5. Computational methods

Density functional theory (DFT) calculations were performed using the Gaussian 16C.01 software. The detailed calculation procedure was described in **Text S3**[25,26].

3. Results and discussion

Several characterisations were carried out to investigate the effect of different carbonisation temperatures on the CQDs. As shown in Fig. 1**a**,

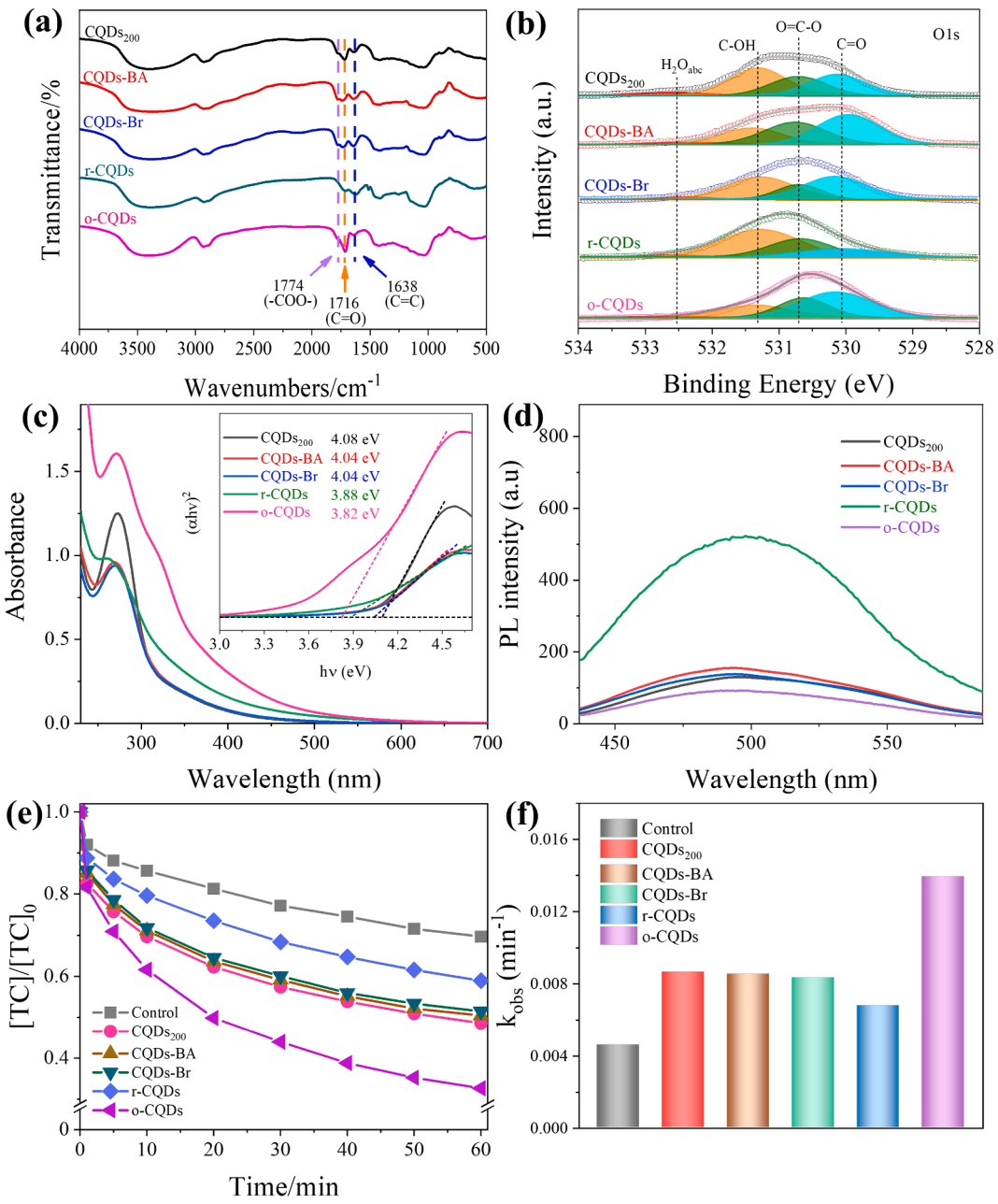

Fig. 2. (a) FT-IR spectra, (b) O1s XPS spectra, (c)UV–vis absorption spectra, (d) Steady PL spectra at 420 nm excitation of $CQDs_{200}$, CQDs-BA, CQDs-Br, r-CQDs and o-CQDs. (e) Comparison of the performance of pristine $CQDs_{200}$ and $CQDs_{200}$ derivatives in PMS activation, (f) Comparison of the apparent reaction rate constants k_{obs}. ($[TC]_0$ = 10 mg/L; [Catalysts] = 0.5 g/L; $[PMS]_0$ = 0.0246 g/L = 0.4 mM; T = 25 °C).

the samples prepared at different carbonisation temperatures all show a broad peak at 19.5°, indicating a distinct amorphous structure corresponding to the (002) plane of carbon[27]. The Raman spectrum (Fig. 1**b**) show that all four samples prepared have a typical D band and a G band at 1350 cm^{-1} and 1592 cm^{-1}, respectively[28]. The intensity ratio of the D band to the G band (I_D/I_G) tends to decrease with increasing carbonisation temperature, which is attributed to the fact that the higher carbonisation temperature may promote dehydration and carbonisation of the carbon source, reducing the content of oxygen functional groups on the surface of the samples and thus reducing defects. The FT-IR spectrum (Fig. 1**c**)showed similar functional groups on the surface of the samples obtained at the four different carbonisation temperatures and two new peaks at 1718 cm^{-1} and 1638 cm^{-1} corresponding to C═O and C═C bonds, respectively.

The XPS measurements results also show that the oxygen content decreases from 42.0% to 18.1% as the carbonation temperature increases from 180 °C to 240 °C (Fig. 1**d** and **Table S1**). Furthermore, the peak area obtained through deconvolution of the O1s XPS spectra could reflect the densities of different O species (Fig. 1**e**)[29]. The high-resolution spectrum of O1s shows four peaks at 532.7, 531.2, 530.7, and 530.1 eV, corresponding to H_2O_{abs}, C-OH, O═C-O and C═O, respectively[30]. Based on the deconvolution results, the content of oxygen functional groups in the different prepared samples can be determined. As can be seen from **Table S1**, the C═O group content of the samples gradually decreases and the O═C-O bond content gradually increases as the carbonation temperature increases. This may be due to the fact that the higher carbonation temperature promotes further oxidation of C-OH groups on maltitol to C═O and then to COOH bonds.

Fig. 1**f** shows the UV–Vis absorption spectra of the four samples. The samples all show a similar strong UV–Vis absorption peak at 285 nm,

corresponding to the π-π* transition in the C═C band and the n-π* transition in the C═O band[31]. As the carbonisation temperature increases, the light absorption capability of the sample gradually increases, suggesting that the conjugated structure in CQDs increased. The UV–vis data were converted using the Kubelka-Munk function, and the band gap energies of the photocatalysts were estimated by linear extrapolation using Tauc plots.The band gaps of $CQDs_{180}$, $CQDs_{200}$, $CQDs_{220}$ and $CQDs_{240}$ were 4.14, 4.08, 4.06 and 3.93 eV, respectively, indicating that increasing the carbonation temperature leads to a narrower band gap for CQDs because of the increase in conjugate structure.

The photoluminescence spectra of $CQDs_{180}$, $CQDs_{200}$, $CQDs_{220}$ and $CQDs_{240}$ changed with a series of excitation wavelength ranging from 280 to 500 nm (**Fig. S1**), which was a typical excitation-dependent PL phenomenon[32]. The excitation-dependent PL behaviour can be determined by the abundant emission traps of surface chemical states formed by different functional groups[33]. Distinct functional groups may generate varying emission traps under specific excitation wavelengths, thus exhibiting the excitation-dependent PL variation. As the carbonization temperature increased, the position of the strongest PL emission peak of CQDs was red-shifted when the excitation wavelength was shifted from 280 to 500 nm, indicating that the absorbance in visible light region was enhanced. In addition, the fluorescence intensity increases accordingly, indicating that the photogenerated charge recombination rate becomes larger, which suppresses carrier separation [34].

To provide a comprehensive evaluation of PMS activation activities in organic degradation performance, TC was selected to evaluate the activation performance of all prepared materials. The degradation reaction was carried out at 25 °C under natural pH conditions. As shown in Fig. 1**g,** the $CQDs_{200}$/PMS/vis system significantly increased the TC removal rate under visible light irradiation compared to other systems, indicating that $CQDs_{200}$ can activate PMS to accelerate the oxidation of TC under light irradiation. As shown in Fig. 1**h**, the TC oxidation rate varies with the carbonation temperature of the sample. $CQDs_{200}$ demonstrates the highest capacity for PMS activation and TC oxidation, in which 51.5% removal of TC was achieved within 60 min. The oxidation efficiency of TC then gradually decreased as the carbonation temperature continued to increase, with removal rates of 43.5% and 38.4% for $CQDs_{220}$ and $CQDs_{240}$ respectively within 60 min. It was intriguingly to note that $CQDs_{180}$ did not follow the above pattern and instead showed the worst performance in activating PMS. The structure was further determined by TEM (**Fig. S2**). Compared with $CQDs_{200}$, the precursor molecules were not fully dehydrated to form a carbon core with conjugated structure at a lower reaction temperature, and the sp^2

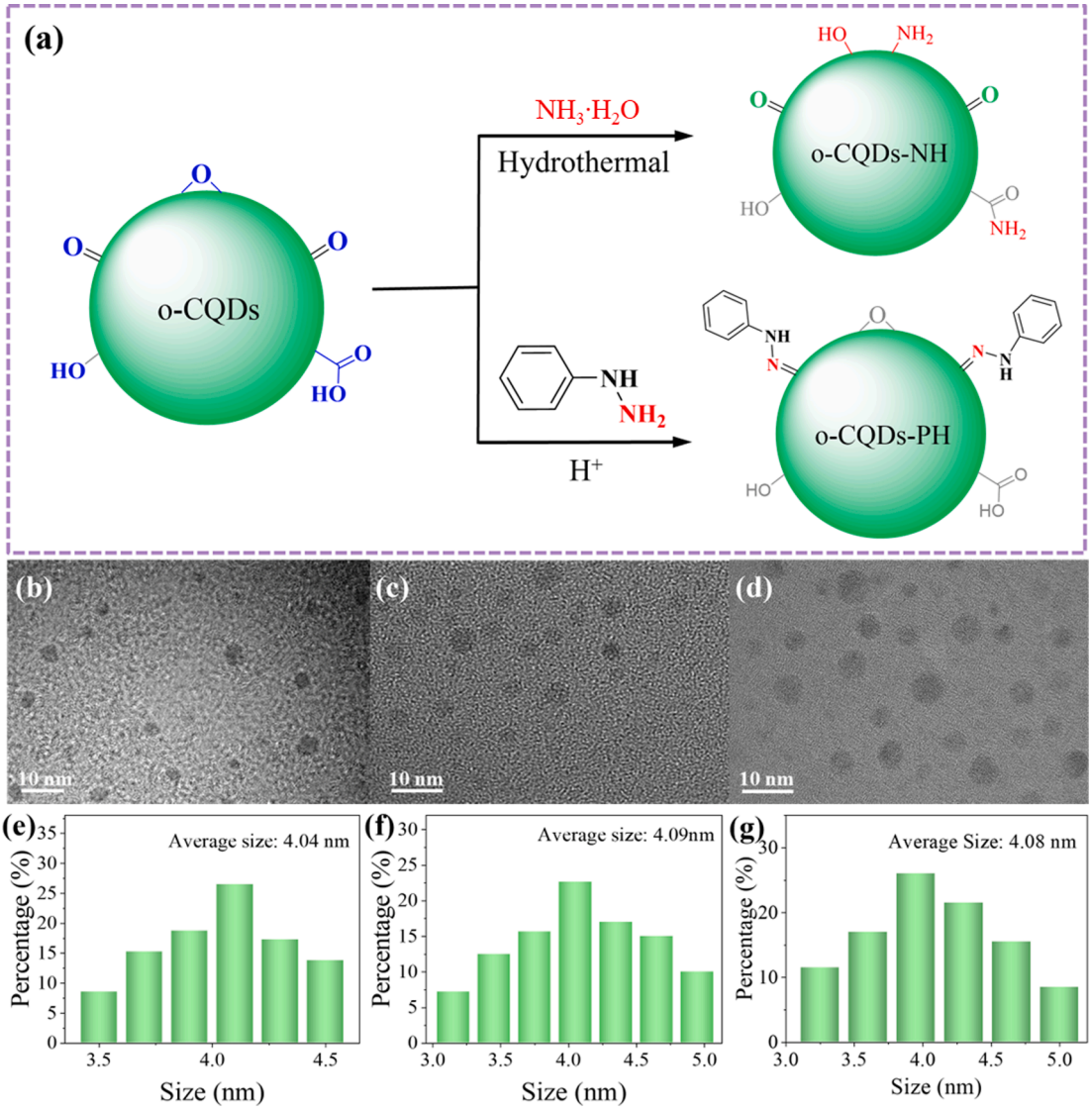

Fig. 3. (a) Schematic diagram of the preparation of o-CQDs and o-CQDs-PH. HRTEM images and particle size distribution of the as-prepared o-CQDs (b, e), o-CQDs-NH (e, f) and o-CQDs-PH (d, g).

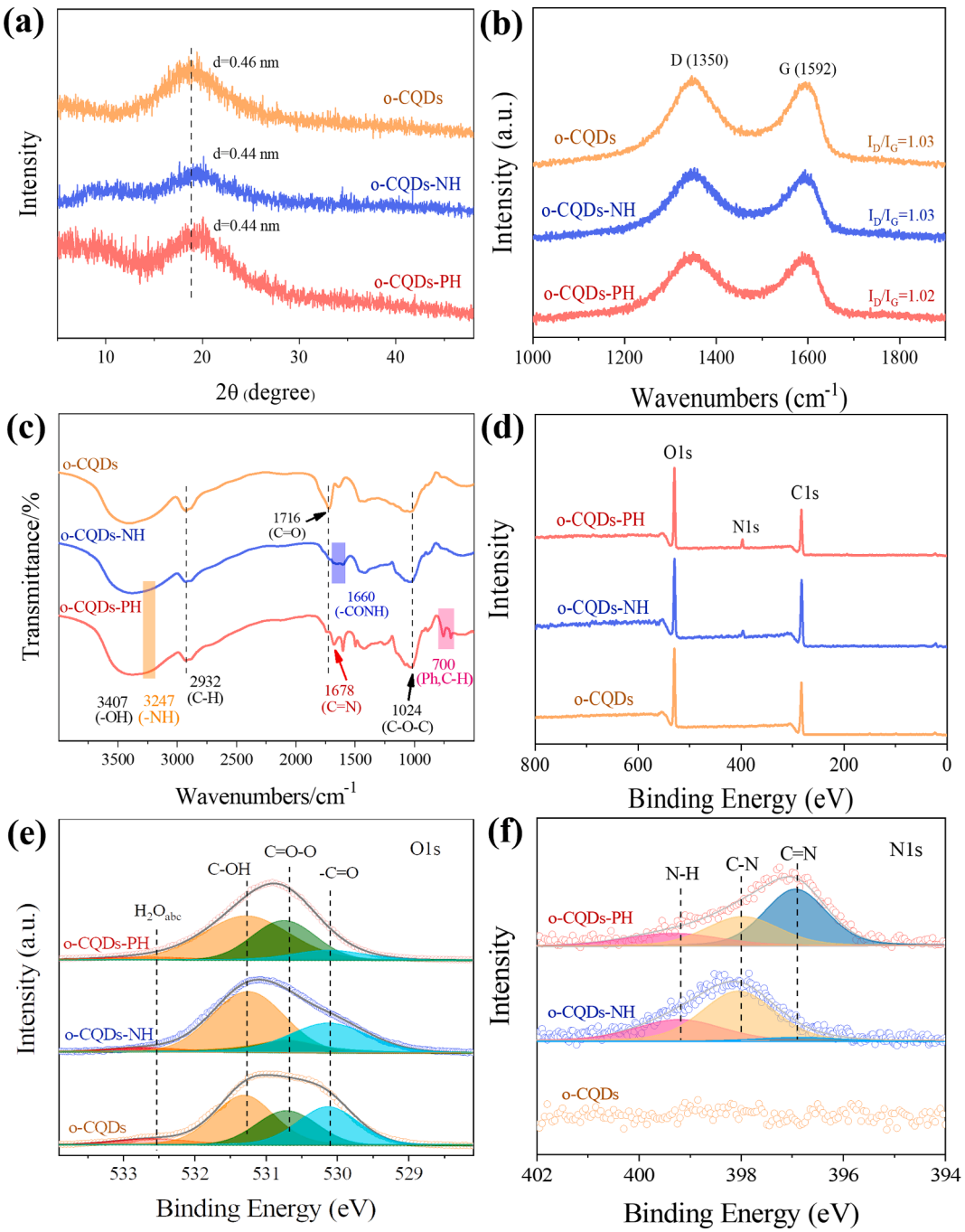

Fig. 4. (a) XRD pattern, (b) Raman spectra, (c) FTIR spectra, (d) The survey XPS spectrum, and (d) high resolution O1s and (d) N1s XPS spectra of the as-prepared o-CQDs, o-CQDs-PH and o-CQDs-NH.

conjugated carbon skeleton of $CQDs_{180}$ is not yet formed. In addition, the excess oxygen groups resulted in poor electrical conductivity and occupation of surface active sites, leading to the prohibited activation of PMS by $CQDs_{180}$. The kinetic calculations in Fig. 1**i** show that the photocatalytic performances of the four samples follows: CQDs200 > CQDs220 > CQDs240 > CQDs180.

Typically, carbonyl groups are active sites for activation of persulfates to generate ROS[35–38]. In addition, the presence of excess carbonyl groups (strong electron-absorbing groups) has also been reported to disrupt the conjugated π system and affect the adsorption and electron transfer processes of the reactants[30]. However, there are no clear reports exploring the effect of C═O groups on CQDs surface for PMS activation. To investigate the effect of C═O groups on the surface of CQDs on the activation of PMS, we established a correlation between the C═O groups and the TC oxidation efficiency using $CQDs_{200}$, $CQDs_{220}$ and $CQDs_{240}$ with different oxygen-containing functional groups. As shown in **Fig. S3**, the C═O group content showed a good positive correlation with the TC removal rate($R^2 = 0.997$). This suggests that the C═O group may be the actual active site for PMS decompostion. This will also be further investigated by chemical titration.

To further identify the active site of activated PMS on $CQDs_{200}$, we performed chemical titration experiments (**Fig. S4**). BA and BrPE were used as the titrants to react specifically with C-OH and COOH groups, respectively[37,38]. $NaBH_4$ can selectively reduce C═O and epoxy to –OH without affecting C═C and –COOH on $CQDs_{200}$[39]. Diss-Martin Periodinane can selectively oxidise –OH to C═O without oxidising

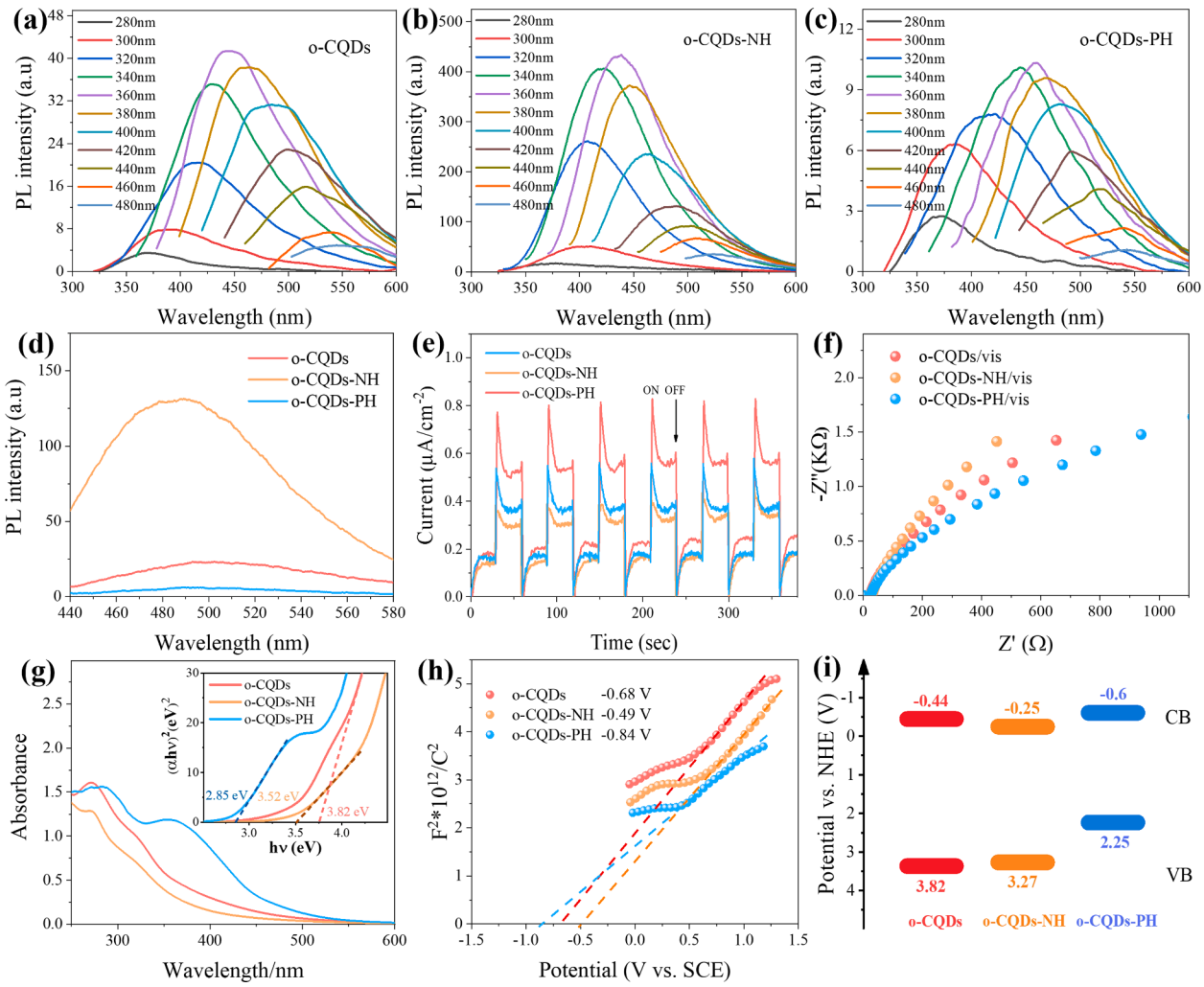

Fig. 5. (a, b, c) Emission properties of o-CQDs, o-CQDs-NH and o-CQDs-PH at different excitation wavelengths from 280 to 480 nm. (d) Steady PL spectra of o-CQDs, o-CQDs-NH and o-CQDs-PH at 420 nm excitation. (e) Transient photocurrent response, (f) EIS Nyquist plots, (g) UV–Vis absorption spectra, corresponding plots of $(\alpha h\nu)^2$ vs band-gap energy ($h\nu$), (h) Mott-Schottky plots, and (i) the estimated band structure alignments of o-CQDs, o-CQDs-NH and o-CQDs-PH.

other species[40,41]. These titration reactions show a high degree of specificity under mild reaction conditions.

The XRD spectra (**Fig. S5**) and Raman spectra (**Fig. S6**) before and after the titration experiments were the same, indicating that the titration reaction of the oxygen functional group had no effect on the crystal structure and morphology. The FT-IR spectra (Fig. 2**a**) show that a small peak is observed at 1774 cm^{-1} for CQDs-BA and CQDs-Br, which is attributed to the formation of ester groups[37]. The intensity of the C═O bond vibration peak of r-CQDs was significantly decreased by $NaBH_4$ reduction. In addition, the C═O signal of o-CQDs became significantly enhanced after treatment with DMP oxidation. The change of oxygen-containing functional groups was further confirmed by XPS spectra measurements after titration reactions. As displayed in O 1 s XPS spectra (Fig. 2**b)** and **Table S2**, for CQDs-BA, CQDs-Br and r-CQDs, the corresponding C-OH, O═C-O and C═O signals decreased substantially, and the C═O signal in o-CQDs increased significantly. Besides, the obtained CQDs derivatives showed absorption spectra (Fig. 2**c**) and photoluminescence spectra (**Fig. S7**) different from that of $CQDs_{200}$. All these results confirmed that the specific titration reaction did occur. Fig. 2**c** also shows that the visible absorption range of o-CQDs improves significantly after the C-OH on the surface of the CQDs is oxidised to C═O by DMP, and that o-CQDs have the smallest band gap values. Steady state photoluminescence (PL) analysis is an effective method for studying the electron-hole pair states reflecting the photocatalytic activity. Fig. 2**d** depicts PL spectra of $CQDs_{200}$ and CQDs-derivatives under 420 nm light excitation. Notably, compared to $CQDs_{200}$, the PL intensity of r-CQDs is significantly enhanced when C═O on the surface of $CQDs_{200}$ is reduced to C-OH. In contrast, the PL intensity of $CQDs_{200}$ decreases when the C-OH is oxidized to a C═O group. This implies that the presence of C═O facilitates the separation of photogenerated electron-hole pairs.

Next, the PMS activation activity of $CQDs_{200}$ derivatives was evaluated. As can be seen in Fig. 2**e and 2f**, compared with $CQDs_{200}$, the TC removal rates of CQDs-BA, CQDs-Br and r-CQDs all decreased, indicating that the titration reaction eliminated some of the active sites. Among them, the catalytic performance of r-CQDs decreased more pronounced, with the TC removal rate decreasing from 51.5% to 41.1%. This suggests that the reduction of C═O or epoxy groups is detrimental to photocatalytic activity in PMS activation. To further verify the function of carbonyl groups, the catalytic activity of o-CQDs was also examined. The results showed that the removal rate of TC in o-CQDs/PMS system increased to 67.4% within 60 min, indicating that the increase in C═O groups promoted PMS activation. As shown in **Fig. S8**, the photocurrent intensities of the five samples were sorted as follows: o-CQDs > $CQDs_{200}$ > CQDs-BA > CQDs-Br > r-CQDs. Compared with C-OH and COOH groups, the reduction of C═O groups cause the greatest decay in the photocurrent. The o-CQDs have the largest photocurrent amplitude, indicating that the increase of C═O groups can promote the

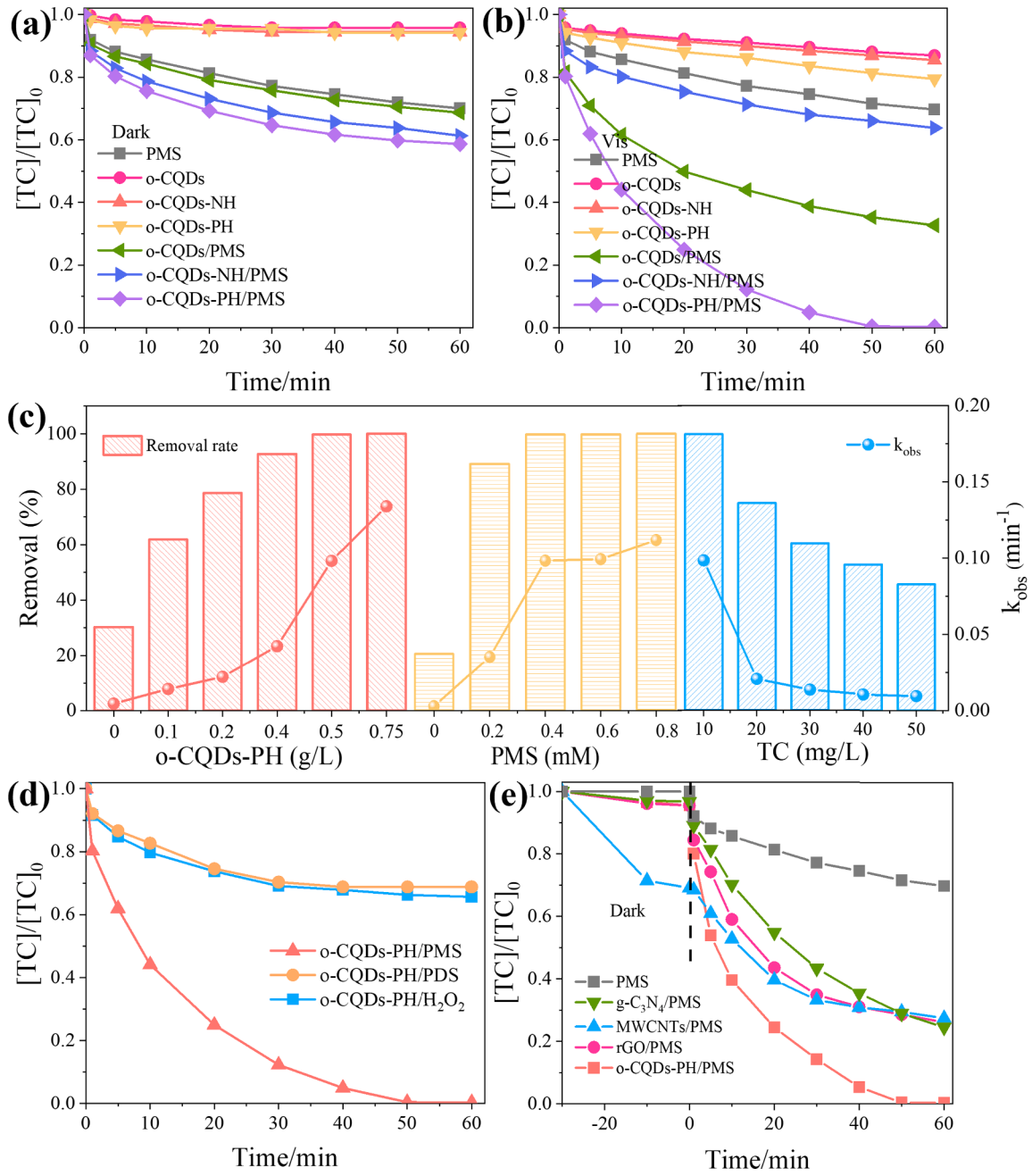

Fig. 6. (a) TC removal or adsorption for the different processes under dark or visible lights (b). (c) Effect of o-CQDs-PH loading, PMS dosage, and initial TC concentration on photodegradation in the o-CQDs-PH/PMS system under visible lights. (d) Catalytic performances of o-CQDs-PH for activating different peroxides under visible lights. (e) Comparing the catalytic activity of o-CQDs-PH with other carbon materials under visible light ($[TC]_0$ = 10 mg/L; [catalyst] = 0.5 g/L, [PMS] = [PDS] = $[H_2O_2]$ = 0.4 mM; pH_0 = 4.8; T = 25 °C).

separation and transfer of photogenerated carrier charges. These results clearly indicate that the C-OH, COOH and C═O groups all contribute to the activity for PMS activation, however the C═O groups are the most active sites.

Considering that pristine CQDs have poor photocatalytic activity in PMS activation because of weak light absorption and sluggish carrier separation kinetics. To further improve the photocatalytic performance of o-CQDs, we used $NH_3{\cdot}H_2O$ and PH as nitrogen sources for the surface chemistry of the modified o-CQDs (Fig. 3**a**). From the HRTEM images in Fig. 3 (b-g), all three prepared samples are well dispersed with a size distribution between 3.0 and 5.0 nm, and the average particle diameter is about 4.0 nm. The HRTEM image results indicate that the surface modification of o-CQDs-NH and o-CQDs-PH would not change the particle size compared with o-CQDs.

As revealed from the XRD pattern (Fig. 4**a**), o-CQDs, o-CQDs-PH and o-CQDs-NH display similar XRD spectra with apparent amorphous structure with a broad peak at 19.5°, corresponding to the (0 0 2) plane. Compared with o-CQDs (1.03), Raman spectroscopy (Fig. 4**b**) shows that the intensity ratio (I_D/I_G) of D band and G band of o-CQDs-PH (1.02) and o-CQDs-NH (1.03) is similar, indicating that the nitrogen modification of o-CQDs surface by PH and ammonia will not produce more defects. In FTIR spectra of o-CQDs (Fig. 4**c**), the stretching frequencies at 3407, 3247, 2932, 1730 and 1024 cm^{-1} are ascribed to –OH, –NH, -C—H, C═O and C—O—C, respectively. Compared with o-CQDs, the infrared spectrum of o-CQDs-PH shows that the vibration peak signal of C═O is significantly reduced, and two obvious vibration peak appeared at 1678

and 700 cm^{-1} after the titration reaction, ascribed to the stretching vibration of the C═N and out-of-plane bending vibration of C—H in the PH group, respectively. In addition, the C═O and C—O—C peaks on the infrared spectrum of o-CQDs-NH significantly weakened, and new peaks emerged for –CONH- at 1660 cm^{-1} and –NH stretching vibrations near 3247 cm^{-1}. The outcome suggests that the oxygen-containing groups (primarily C═O and C—O—C) on the surface of o-CQDs reacted with ammonia and formed amine groups on the surface. These results are consistent with the literature reports[42,43]. XPS measurements were performed to further analyse the surface chemical composition and states of the as-prepared o-CQDs, o-CQDs-PH and o-CQDs-NH. As displayed in the XPS survey spectra (Fig. 4**d**), C, N and O elements can be seen in o-CQDs-PH at 284.3, 397.0 and 530.2 eV, respectively. The presence of N elements in o-CQDs-PH and o-CQDs-NH are further verified by the high-resolution N1s spectra (Fig. 4**f**), demonstrating that PH and $NH_3{\cdot}H_2O$ have successfully reacted with o-CQDs and are drafted on the surface. As displayed in O 1 s XPS spectra (Fig. 4**e**), the decreases in the intensities of the C═O signal for o-CQDs-PH indicated that the reactions had indeed occurred. In addition, compared with o-CQDs, the contents of C—O—C and –COOH on the surface of o-CQDs-NH were significantly reduced, because partial C—O—C and –COOH on the surface of o-CQDs reacted with the reductive chemicals to form $–NH_2$ and –CONH-[44].

To measure the optical absorption properties of the samples and to explore their energy band structures. Compared with o-CQDs (Fig. 5**a**), when the excitation wavelength was shifted from 280 to 480 nm, the half-peak width of PL emission peak of o-CQDs-NH was phenomenally narrower and the fluorescence intensity was significantly higher (Fig. 5**b**), and the PL emission peak of o-CQDs-PH had a significant red shift and reduced intensity (Fig. 5**c**). In addition, the fluorescence quantum yields of o-CQDs, o-CQDs-NH and o-CQDs-PH were 2.36, 11.63 and 0.31%, respectively (**Table S3**). These results indicate that the modification of ammonia water and phenylhydrazine changes the surface state of o-CQDs, thereby exhibiting different emission properties [45]. The PL (Fig. 6**d**) results suggest that all three samples exhibit a broad peak at around 500 nm, which can be ascribed to the radiative recombination between excited electrons and holes. Compared with o-CQDs, the PL intensity of o-CQDs-NH increased significantly, and the reaction between NH_3 and o-CQDs promoted the recombination of photogenerated charge carriers. Epoxy and carboxyl groups are the center of non-radiation recombination, and ammonium can proceed with a nucleophilic reaction to remove the epoxy and the carboxyl groups. Therefore, a great portion of C—O—C and –COOH groups reacted react with the ammonia under heating conditions to generate new functionalities of –OH, $–NH_2$ and –CONH-, which reduces non-radiative recombination and enhances the fluorescence intensity of o-CQD-NH; but this is not conducive to the photocatalytic reaction[46]. And the spontaneous surface polarization caused by PH functionalization, the electrons and holes on o-CQDs are spatially separated, which leads to the decreased PL intensity of o-CQD-PH.

Furthermore, as shown in Fig. 5**e**, o-CQDs-PH exhibits the improved photocurrent responses compared with o-CQDs and o-CQDs-NH, indicating that the introduction of pH increased the density and migration of photogenerated carriers. Electrochemical impedance spectroscopy (EIS) was used to reflect the electronic conductivity and interfacial charge transfer behaviour of catalysts (Fig. 5**f**). The EIS of o-CQDs-PH showed the smallest semicircle diameter, indicating a lower charge transfer resistance of o-CQDs-PH, which implies that o-CQDs-PH allows faster charge transfer by separating electrons and holes.

The UV–Vis absorption spectra of o-CQDs, o-CQDs-NH and o-CQDs-PH are shown in Fig. 5**g**. All three samples showed a similar strong UV–Vis absorption peak at 285 nm, corresponding to the π-π* transition of the C═C band and the n-π* transition of C═O band. Compared with o-CQDs and o-CQDs-NH, the absorption edge of o-CQDs-NH is red-shifted with a stronger absorption peak at 355 nm, which may be attributed to the n-π* transition of the C═N bond on o-CQDs-PH. This indicates that the introduction of pH helps to improve the visible light absorption for o-CQDs. As shown in Fig. 5**g** (inset), the band gaps of o-CQDs, o-CQDs-NH and o-CQDs-PH were 4.08, 3.52 and 2.85 eV, respectively, indicating that the surface nitrogen modification leads to a narrower band gap of o-CQDs.

Fig. 5**h** shows that o-CQDs, o-CQDs-NH and o-CQDs-PH are determined as *n*-type semiconductors according to the positive slope of the Mott-Schottky diagram. Since the flat band of the *n*-type semiconductor is located at a position close to the conduction band (CB), according to the equation $E_{NHE} = E_{SCE} + 0.24$, the E_{CB} values of o-CQDs, o-CQDs-NH and o-CQDs-PH are determined to be −0.44, −0.25 and −0.60 V vs NHE, respectively. The valence band (VB) potential of the sample can be determined according to the equation $E_{VB} = E_{CB} + E_g$, where E_{VB} and E_{CB} represent the potential of CB and VB, respectively, and E_g represents the band gap energy. Based on these results, the energy level diagrams of o-CQDs, o-CQDs-NH and o-CQDs-PH are displayed in Fig. 5**i**, in which o-CQDs-PH illustrates a narrower band gap and an upward shift of the energy band position. The introduction of pH onto the surface of o-CQDs can fine-tune its electronic structure, on the one hand narrowing the band gap to enhance light absorption and facilitating the separation of photogenerated electron-hole pairs. On the other hand, the upward shift of the conduction band position facilitates the transfer of photogenerated electrons to the PMS. Therefore, it is beneficial to enhance the activation performance of PMS under visible light irradiation.

3.1. Photocatalytic activity

TC degradation in different oxidation processes was measured to evaluate the adsorption and photocatalytic capacities of o-CQDs, o-CQDs-PH and o-CQDs-NH. Firstly, The removal of TC in different systems in dark conditions was investigated. In Fig. 6**a**, the adsorption capacity of the three samples on TC was similar. This excluded the contribution of TC adsorption to their performance comparison. In addition, the degradation rate of TC by PMS alone was relatively slow both in dark (29.9%) or under visible light (30.4%), indicating that PMS could not be activated by visible light. The removal rates of TC by o-CQDs/PMS, o-CQDs-NH/PMS and o-CQDs-PH/PMS were 31.4%, 38.7% and 41.4% within 60 min in dark, respectively. This indicates that the introduction of electron-rich N functionality on the o-CQDs surface promotes direct electron transfer to PMS for activation to generate reactive species for TC removal. Compared with o-CQDs/PMS/Vis system (45.9%) (Fig. 6**b**), the degradation rate of TC by o-CQDs-PH/PMS/Vis system was significantly increased to 99.7%, which was attributed to the enhanced light absorption and photogenerated carrier separation by o-CQDs-PH, as evidenced by Fig. 5**d and 5e**. However, the degradation rate of TC by o-CQDs-NH/PMS/vis system decreased (36.3%), due to the rapid recombination rate of electron-hole pairs of o-CQDs-NH, which inhibited the photogenerated carrier separation and thus reduced the photocatalytic performance.

The effect of o-CQDs-PH dosage on TC removal in the CQDs-PH/PMS system is depicted in Fig. 6**c**. As the o-CQDs-PH concentration increased in the range of 0 to 0.75 g/L (0, 0.1, 0.2, 0.4, 0.5, and 0.75), the TC removal efficiencies were 30.4%, 61.9%, 78.7%, 92.7%, 99.7%, and 99.8%, respectively. The increase in removal efficiency was attributed to the increased number of available active sites to react with PMS, thereby generating more ROS. In contrast, catalysts with concentrations greater than 0.5 g/L have a negligible effect on promoting TC degradation. This can be explained by the fact that an excess of catalyst hinders the light penetration in the reactor and reduces the irradiated surface area, thus decreasing the overall photocatalytic efficiency of the process. Therefore, considering the catalyst efficiency, 0.5 g/L was used as the optimal dose for subsequent experiments.

The effect of PMS concentration on TC removal in the o-CQDs-PH/PMS system was also investigated. Fig. 6**c** shows TC removal as a function of different concentrations of PMS (0–0.8 mM). As the PMS concentration increased from 0 to 0.4 mM, TC degradation was

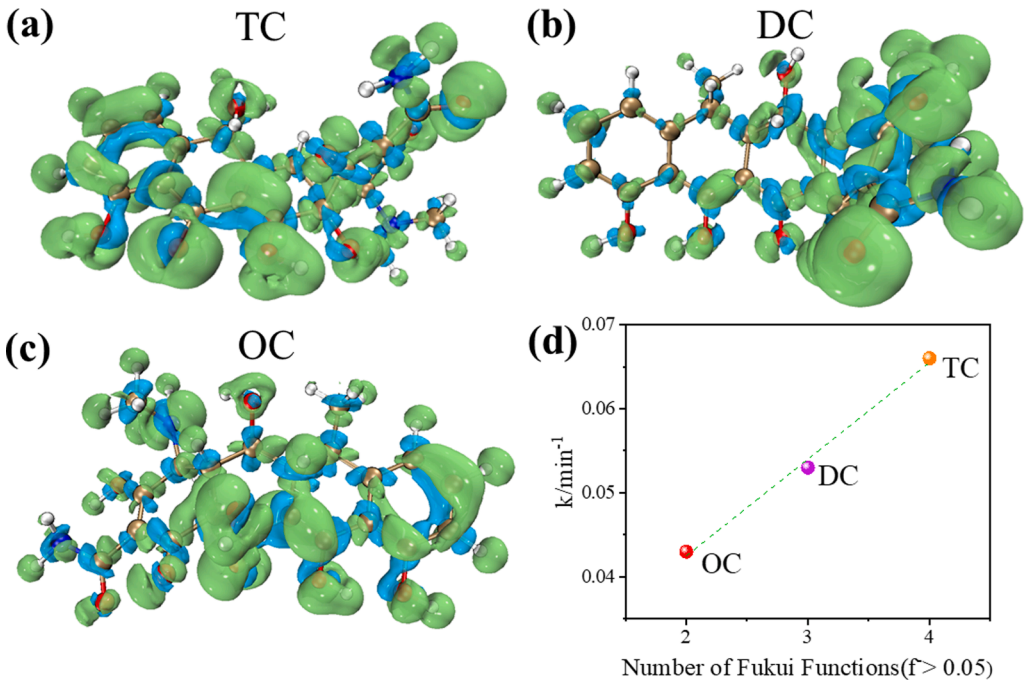

Fig. 7. f^- Fukui indexes image of TC (a), DC (b), and OC (c); (d) Correlation of Pseudo-first order kinetic constants (k) of different organics with its Fukui index (f^-) ($[DC]_0 = [OC]_0 = 20.7$ μM; [o-CQDs] = [o-CQDs-NH] = [o-CQDs-PH] = 0.5 g/L; $[PMS]_0 = 0.0246$ g/L = 0.4 mM; $pH_0 = 4.8$; T = 25 °C).

gradually accelerated. When the PMS concentration was further increased to 0.8 mM, the k_{obs} value for TC removal essentially ceased to increase. This is because the high concentration of PMS affects the adsorption of TC on the catalyst as well as quenches the reactive species [47].

The photocatalytic performance on TC removal in the o-CQDs-PH/PMS system was investigated at different initial concentrations of TC from 10 to 50 mg/L (Fig. 6**c**). With the increase of TC concentration from 10 to 20, 30, 40 and 50 mg/L, the TC removal rate gradually decreased, and the degradation efficiencies were 99.7%, 74.9%, 60.4%, 52.7% and 45.6%, respectively. At low TC concentrations, the effective photocatalytic reaction between TC molecules and the catalyst is higher because both o-CQDs-PH and PMS are excessive. As TC concentration increases, the rapid exhaust of PMS and the generated ROS leads to competition between TC and large amounts of decolorized intermediates, thus prohibiting the TC degradation.

The catalytic activity of o-CQDs-PH was evaluated for activating different peroxides for TC oxidation (Fig. 6**d**). Compared with the moderate activity with PDS (31.2%) and H_2O_2 (34.4%), o-CQDs-PH shows particular activity toward PMS and achieves 99.7% of TC degradation in 60 min. A similar scenario was reported in other AOP systems, in which boron and carbon nanotubes (CNTs) are more active to activate PMS than PDS or H_2O_2[48,49]. This is because the asymmetric molecular structure of PMS is more vulnerable to be catalytically decomposed, resulting in unbalanced electron distribution to evolve reactive species.

To examine the reusability of o-CQDs-PH, the cyclic TC degradation performance of the o-CQDs-PH/PMS system was tested under visible light irradiation. As shown in **Fig. S9**, the TC degradation rate decreased from 99.7% to 71.9% after five consecutive runs, which was attributed to the adsorptive coverage of active site by degradation intermediates and corrosion of o-CQDs-PH surface by ROS, which reduces the oxidation efficiency.

The catalytic performance of o-CQDs-PH was compared with that of other metal-free carbon materials. As illustrated in Fig. 6**e**, compared with the presence of PMS alone, graphitic carbon nitride (g-C_3N_4), pristine multi-walled carbon nanotubes (MWCNT) and reduced graphene oxide (rGO) attained 3.3%, 30.9%, and 4.5% pollutant removal in dark. Under light irradiation, the removal efficiencies of g-C_3N_4, MWCNT and rGO are significantly improved, achieving 75.6%, 72.6%, and 73.9%, respectively. In contrast, in the o-CQDs-PH/PMS system, TC degradation reached 4.5% in dark in the first 30 min and increased to 99.7% under visible illumination in 60 min. The outcomes indicate that o-CQDs-PH have higher performances for persulfate activation in both catalytic and photocatalytic processes.

The degradation of DC and OC was also examined to evaluate the oxidation capacity in various catalytic processes. As depicted in Fig. S10**b and s10c**, the degradation rate of DC and OC by o-CQDs-PH/PMS system remained above 90%. within 60 min. Pseudo-first-order kinetic fits were performed for the degradation curves of different organics within 30 min. The degradation kinetic constants of TC, DC and OC were 0.067, 0.053, and 0.043 min^{-1} in o-CQDs-PH/PMS/TC, o-CQDs-PH/PMS/DC and o-CQDs-PH/PMS/OC systems, respectively. The different degradation rates in o-CQDs-PH/PMS system indicated substrate-specific reactivity[50]. Due to the different electron-donating abilities of organics, the oxidative degradation rates of different organics were also different during ROS oxidation. Fukui function (f^-) was often used to measure the feasibility of an organic matter to lose electrons. The higher the f^- value of the atom in the molecule, the easier it was to lose electrons and experience oxidation reactions[51,52]. It was assumed that positions with f^- values greater than 0.05 were the active sites where organics were prone to be oxidized, and the greater the number of sites, the higher likelihood that organic molecules would lose electrons upon contacting with ROS. As shown in Fig. 7**a-c**, the Fukui functions (f^-) of TC, DC and OC were calculated, and the detailed values are listed in **Table S5-S7**. In TC, DC, and OC, the number of sites with f^-values greater than 0.05 for atoms are 4, 3, and 2, respectively. Fig. 7**d** shows the relationship between the k values of the three organics and the number of sites susceptible to oxidation reactions. As the number of oxidation sites increases, the k values of organics also increase sequentially, showing a well-fitted positive correlation, which indicates that the degradation performance of the organics depends on the number of oxidation sites. This provides a new insight into the different degradation behaviors of organics by advanced oxidation.

To determine the generated ROS responsible for photocatalytic degradation of TC, radical trapping experiments were performed. Silver

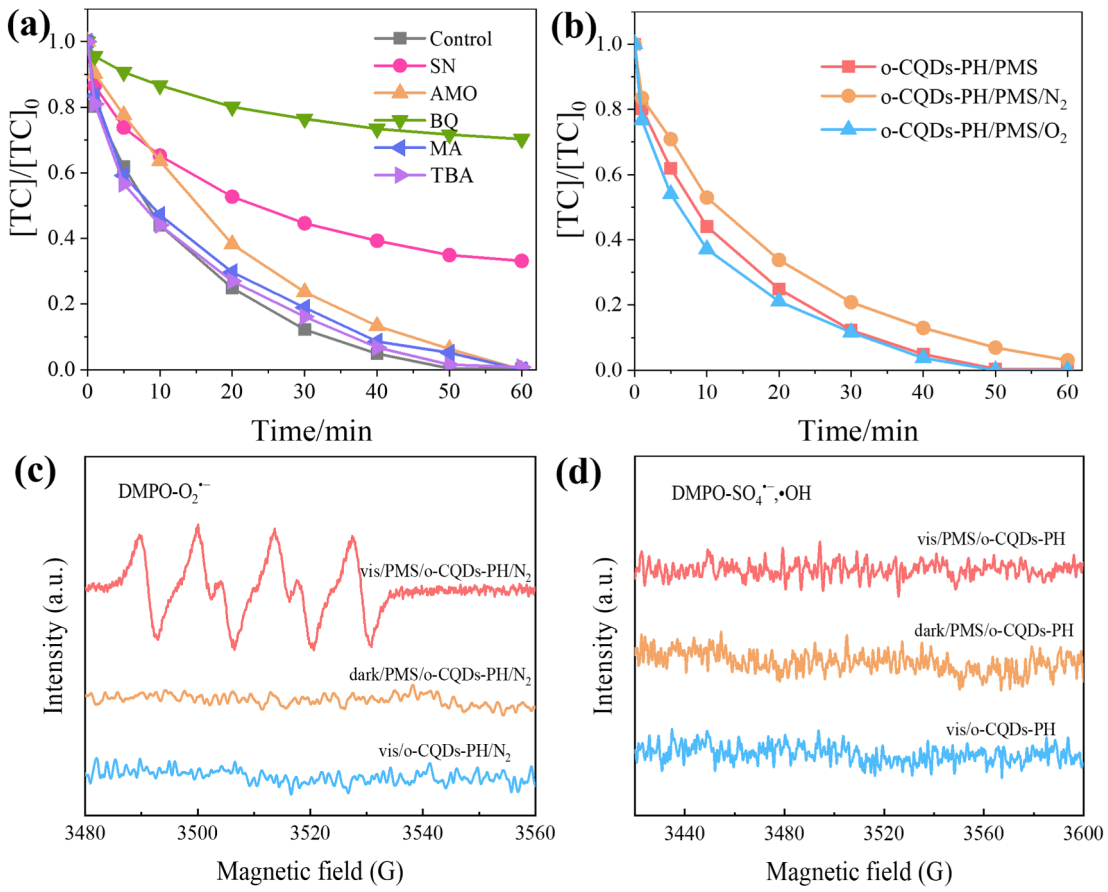

Fig. 8. (a) Effect of various quenchers on TC degradation in o-CQDs-PH/PMS system. (b) Effects of N_2 or O_2 atmosphere on TC decomposition in o-CQDs-PH/PMS system under visible light irradiation. ESR spectra of (c) $O_2^{\bullet-}$, (d) $SO_4^{\bullet-}$ and •OH under different reaction conditions. ([TC] = 10 mg/L, [o-CQDs-PH] = 0.5 g/L, [PMS] = 0.4 mM, [SN] = 4 mM, [AMO] = 40 mM, [BQ] = 20 mM, [MA] = [TBA] = 400 mM).

nitrate (SN), ammonium oxalate (AMO) and p-benzoquinone (BQ) were often used as scavengers to capture photogenerated electrons (e^-), holes (h^+) and superoxide anion radicals ($O_2^{\bullet-}$), respectively. Methanol (MeOH) is used as a scavenger for sulfate radicals ($SO_4^{\bullet-}$) and hydroxyl radicals (•OH), and *tert*-butanol (TBA) is engaged as a scavenger of •OH. Furfuryl alcohol (FFA) and 2,2,6,6-tetramethyl-4-piperidinol (TMP) as the scavengers for singlet oxygen ($^1O_2$). First, the effect of various quenchers on PMS consumption was investigated to exclude the decrease in TC degradation due to the direct consumption of large amounts of PMS by these reductive reagents. As depicted in **Fig. S11**, compared to other quenchers that did not significantly consume PMS, the content of PMS decreased rapidly in the presence of TMP and FFA, the expenditure percentages of PMS by TMP and FFA alone reached 54.4 % and 63.7 % in 60 min, respectively. Due to the rapid consumption of PMS by two quenchers, $^1O_2$ could not be determined as the dominant ROS in the o-CQDs-PH/PMS system. Furthermore, we used solvent exchange experiment based on the longer lifetime of $^1O_2$ in D_2O (20–32 μs) than in H_2O (2 μs). The outcome shows that the degradation kinetics of the o-CQDs-PH/PMS system in D_2O or H_2O solutions are similar, and thus, singlet oxygenation is not the primary oxidation pathway in the o-CQDs-PH/PMS system (**Fig. S12**)[53]. In contrast (Fig. 8**a**), BQ showed the strongest inhibition of TC degradation in the o-CQD-PH/PMS system, indicating that $O_2^{\bullet-}$ may play an important role in TC degradation. In addition, the addition of SN inhibited TC degradation in the o-CQD-PH/PMS system because the addition of SN consumed photogenerated electrons and hindered PMS activation. However, the presence of AMO slightly inhibited the degradation of TC, and the complete removal of TC was attained in 60 min. This is probably because the depletion of h^+ also reduces the charge carriers' recombination and partially compensates the oxidation efficiency. Thus, the accumulated e^- will accelerate the activation of PMS and generate more ROS, thus promoting the degradation of TC. However, the introduction of MA and TBA had essentially no effect on the degradation of TC, indicating that $SO_4^{\bullet-}$ and •OH are not the primary ROS in the o-CQD-PH/PMS system.

To determine the source of $O_2^{\bullet-}$, the photocatalytic degradation of TC by CQD-PH/PMS under N_2 or O_2 atmosphere was investigated, and the results are shown in Fig. 8**b**. The TC degradation rate decreased slightly under N_2 atmosphere, and the TC degradation rate only increased slightly under O_2 atmosphere in the CQD-PH/PMS process, which means that dissolved oxygen might participate in the evolution of active species but its contribution was insignificant. ROS ($O_2^{\bullet-}$) is mainly generated from PMS activation due to the higher electrophilicity of PMS compared with molecular oxygen. Thus, the system is highly effective for wastewater treatment under anaerobic conditions. The ROS involved were further confirmed by in-situ EPR spectroscopy. Fig. 8**c** shows the characteristic ESR signal of DMPO-$O_2^{\bullet-}$ adducts in vis/PMS/o-CQDs-PH/N_2 system, which indicates that o-CQDs-PH activates PMS to generate $O_2^{\bullet-}$ under visible light irradiation rather than from oxygen. In addition, the signals of DMPO-$SO_4^{\bullet-}$ and DMPO-•OH were not observed in various systems in Fig. 8**d**, indicating that o-CQDs-PH could not activate PMS to produce $SO_4^{\bullet-}$ or •OH.

To explore the effect of surface states on the electronic structure of CQDs, the density functional theory (DFT) and time-dependent DFT (TD-DFT) method were used to calculate the surface electronic/orbital culture of o-CQDs, o-CQDs-NH and o-CQDs-PH, including the highest occupied molecular orbit (HOMO), the lowest unoccupied molecular orbit (LUMO) and the distribution of electron holes (Fig. 9).

Previous studies have shown that the change of surface state can

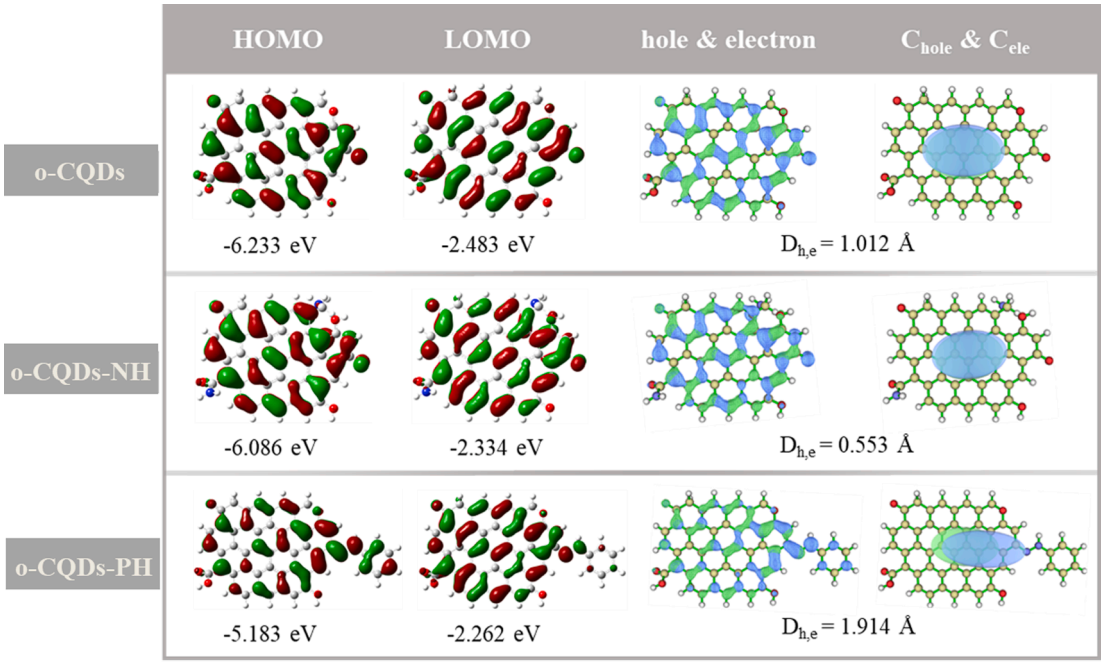

Fig. 9. The distribution of the HOMOs and LUMOs and real space representation of hole and electron distributions and centroids at the S0 → S1 excited state. ($D_{h,e}$: The centroid distance of electron and holes).

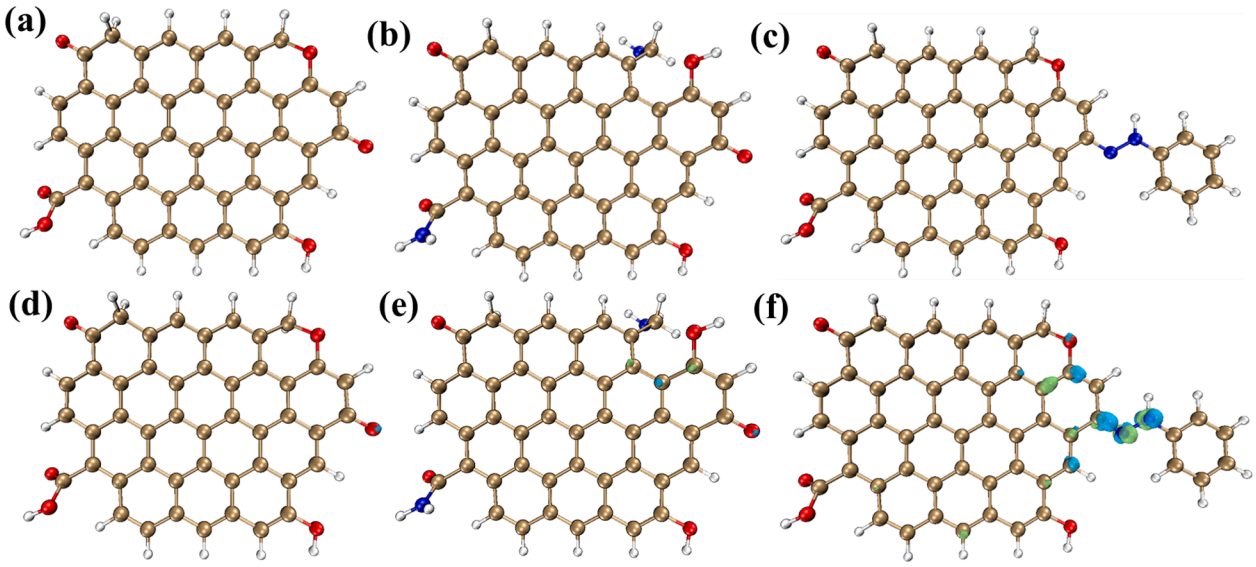

Fig. 10. The chemical structure (a) o-CQDs, (b) o-CQDs-NH, and (c) o-CQDs-PH (Red, oxygen; blue, nitrogen; yellow, carbon; white, hydrogen). Fukui function CDD of (d) o-CQDs, (e) o-CQDs-NH, and (f) o-CQDs-PH (Isovalue = 0.003; The green and blue colors represent the positive and negative phases of the molecular orbital). (For interpretation of the references to color in this figure legend, the reader is referred to the web version of this article.)

change the energy gap of CQDs between HOMO and LUMO. Therefore, HOMO and LUMO of o-CQDs-PH was calculated. Fig. S13 showed that the electronic structures of HOMO and LUMO changed significantly after nitrogen-modification of the o-CQDs surface. Specifically, the orbital position of o-CQDs-PH was lifted up, and the energy gap (difference between LUMO and HOMO) of o-CQDs-PH was 2.921 eV, lower than o-CQDs (3.750 eV) and o-CQDs-NH (3.752 eV), indicating that o-CQDs-PH has higher photo-absorption capacity and can leverage a broader light range, which is consistent with the characterization and photocatalytic activity tests. In addition, the up-shift of the LUMO of CQDs-PH would thermodynamically facilitate the transfer of photo-generated electrons for PMS activation and ROS evolution[47].

To further investigate the change of photocatalytic activity with the change of surface state, time-dependent DFT calculation was used to analyze the electron-hole distributions on o-CQDs-PH at the S0 → S1 excited state. $D_{h,e}$ is expressed as the distance between the centroids of electrons and holes, reflecting the separation effect of electrons and holes[26]. Compared with o-CQDs, the distribution of electrons and holes on the surface of o-CQDs-NH is uniform, the distribution areas of electron-hole pairs are almost completely overlapped, and the D index is reduced from 1.012 to 0.553 Å, which indicates that the reduction of carboxyl groups and epoxy groups in the non-radiation center promotes the recombination of electron-hole pairs after ammonia modification. However, the introduction of pH greatly changed the distribution of electrons and holes on the surface, causing the D index to increase significantly from 1.012 to 1.914 Å. The phenomenon suggests the

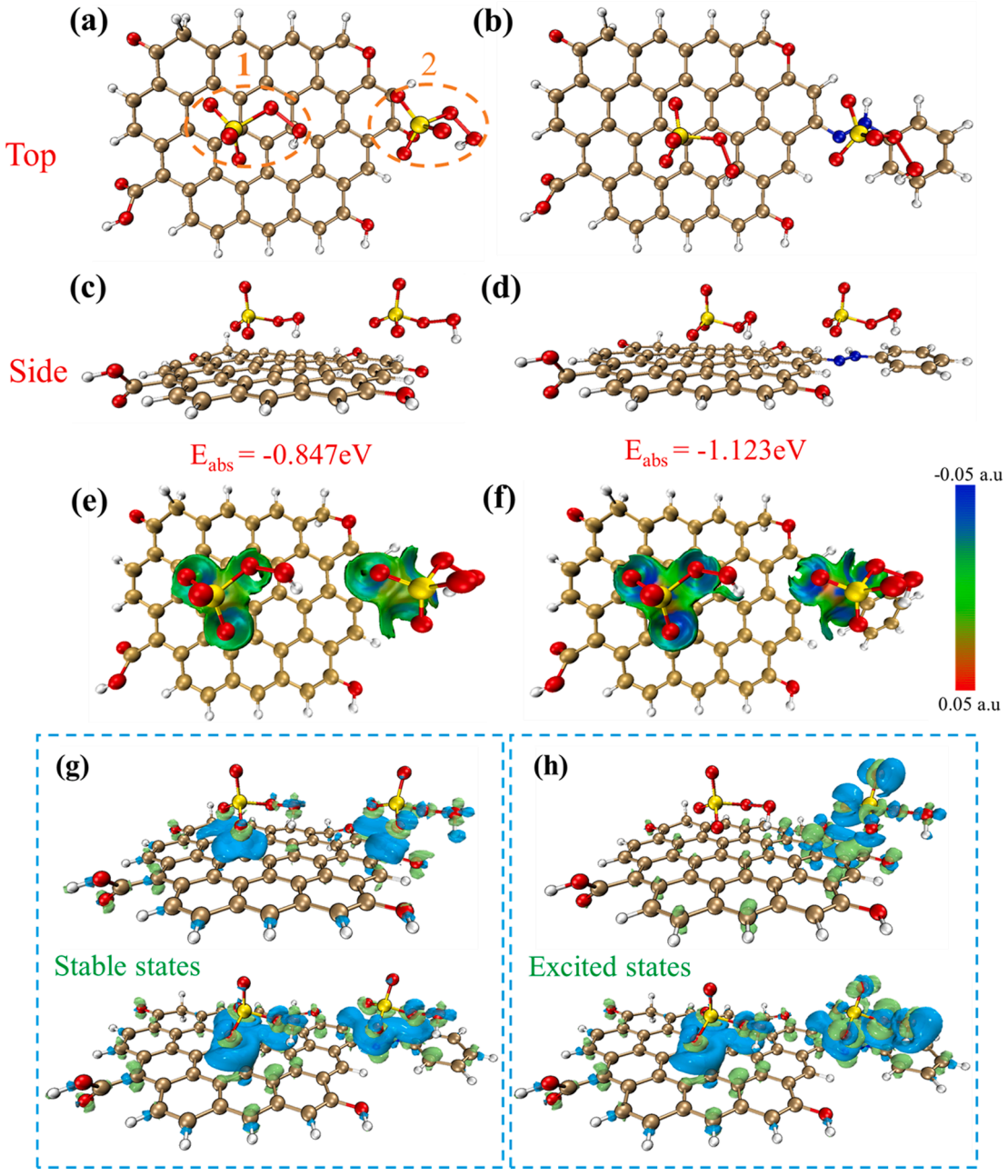

Fig. 11. PMS adsorption onto o-CQDs (a, c) and o-CQDs-PH (b, d). Sign(λ_2)ρ colored isosurfaces of δg^{inter} = 0.01 a.u. corresponding to IGMH analyses for o-CQDs/PMS (e) and o-CQDs-PH/PMS (f). Three-dimensional charge density difference of o-CQDs/PMS and o-CQDs-PH/PMS molecule (g). The charge density difference (ρ_{TS}) in the first excited states (h). (The blue color represents the electron depletion region and the green color represents the electron accumulation region). (For interpretation of the references to color in this figure legend, the reader is referred to the web version of this article.)

efficient separation of electron-hole distribution, which was conducive to the electron transfer to PMS at the electron-rich site and accumulating holes for direct hole oxidation of organic pollutant.

To further analyze the changes in the electronic structure of o-CQDs caused by the introduced nitrogen functionality and to observe the transfer trends of electrons and active sites, the local structure of the graphene model of o-CQDs was analyzed using the Fukui function[34]. By adding one electron ($\rho(N+1)$) or subtracting one electron ($\rho(N-1)$) to the constructed structural model, the charge transfer inside the molecule was speculated by theoretically calculating the electron-gain/-loss capacity of individual atoms in the material molecule. The Fukui index isosurfaces for o-CQDs, o-CQDs-NH and o-CQDs-PH are presented in **Fig. S14**. In addition, the Fukui function compressed double descriptor (CDD) isosurfaces of o-CQDs, o-CQDs-NH and o-CQDs-PH are also compared in Fig. 10. Compared to o-CQDs and o-CQDs-NH, the charge distribution of o-CQDs-PH changes significantly, and the C═N-N group region is tightly surrounded by Fukui index isotopes, indicating that the introduction of pH changes the electronic structure of o-CQDs. As seen in **Table S8**, the absolute value of the CDD of the secondary amine N atom (0.0277) in the PH group is the largest. In addition, the electron loss capacity of each atoms was examined with f^- to simulate the electron distribution within the material during the photocatalytic reaction. The highest f^- value (0.0476) was found for the secondary amine N atom in the PH group, indicating that the secondary amine N atom is the predominant active site. Simultaneously, there is a tendency forelectron to transfer from the graphitic domain of o-CQDs to the PH group. Thus, the introduction of the PH group leads to the directional transfer of local charges on the o-CQDs surface, while the C═N-N bond serves as a bridge

Table 1
Adsorption energy (E_{ads}) and bond length of S—O and O—O in o-CQDs and o-CQDs-PH.

System	$l^1_{s\text{-}o}$ (Å)	$l^1_{o\text{-}o}$ (Å)	$l^2_{s\text{-}o}$ (Å)	$l^2_{o\text{-}o}$ (Å)	E_{abs} (eV)
free PMS	1.735	1.456	1.735	1.456	–
o-CQDs	1.734	1.439	1.755	1.434	−0.847
o-CQDs- PH	1.728	1.436	1.783	1.454	−1.123

for charge migration to accelerate the electron transfer and surface redox reactions.

The PMS activation processes of o-CQDs on the graphite domains and carbonyl or PH groups of o-CQDs before and after phenylhydrazine modification are shown in Fig. 11**a and 11b**. The adsorption energies (E_{ads}), O—O bond ($l_{o\text{-}o}$) and S—O ($l_{s\text{-}o}$) bond lengths of PMS at different positions were calculated. The specific values are shown in Table 1, compared with the $l_{o\text{-}o}$ values of free PMS (**Fig. S15**), the $l_{o\text{-}o}$ bond values of PMS on both o-CQDs and o-CQDs-PH show different degrees of reduction, which indicates that PMS cannot be directly decomposed into $SO_4^{\bullet-}$ and •OH. This is consistent with the radical quenching experiments. Moreover, the enlargement of $l_{s\text{-}o}$ follows the order of o-CQDs-PH($l^2_{s\text{-}o}$) > o-CQDs($l^2_{s\text{-}o}$) > free PMS($l^2_{s\text{-}o}$) > o-CQDs ($l^1_{s\text{-}o}$) > o-CQDs-PH($l^1_{s\text{-}o}$), indicating that both the carbonyl group on o-CQDs and the PH group on o-o-CQDs-PH can help stretch the S—O bond, where o-CQDs-PH($l^2_{s\text{-}o}$) exhibited the longest $l^2_{s\text{-}o}$ (1.783 A), suggesting that PMS may first tend to generate $HO_2^{\bullet}$ and then further decompose to generate $O_2^{\bullet-}$. In addition, the E_{ads} value for PMS increased from −0.847 (pristine o-CQDs) to −1.123 eV after PH modification, indicating that o-CQDs-PH exhibited better PMS adsorption ability, which contributes to the subsequent activation (cleavage and charge transfer)[54]. To show the interaction between o-CQDs and PMS more intuitively, independent gradient model based on Hirschfeld partition (IGMH) analysis was performed using Multiwfn[55]. Fig. 11**e and 11f** shows the IGMH plots of o-CQDs/PMS and o-CQDs-PH/PMS, where PMS and o-CQDs or o-CQDs-PH each defined as a fragment. There is a significant attraction in blue, indicating the presence of a specific interaction, a van der Waals interaction (dispersion-dominated physisorption) with less attraction in green, and red is a strong repulsive interaction. Comparing o-CQDs/PMS, the O atoms on PMS are in darker blue in the center of the equivalence plane with o-CQDs-PH, suggesting that the introduction of pH can effectively modulate the electronic structure to facilitate PMS adsorption, thus improving the activation of PMS. Subsequently, three-dimensional charge density difference analysis revealed the electron transfer between o-CQDs (or o-CQDs-PH) and PMS (Fig. 11**g**). In both o-CQDs/PMS and o-CQDs-PH/PMS systems, the electron depletion region is concentrated on the photocatalyst, while electrons are clustered on the O atoms of PMS, leading to a tendency of electron transfer from o-CQDs or o-CQDs-PH to PMS. In addition, the charge density difference (ρ_{TS}) in the first excited states was calculated (Fig. 11***h***). The C═O group on o-CQDs in the excited state has a clear tendency to transfer electrons to PMS, which demonstrates that the C═O group is the active site for PMS activation. However, the PH group in o-CQDs-PH in the excited state exhibits a stronger tendency to transfer electrons to PMS. Benefiting from the modulation of the electronic structure, the graphite domains in o-CQDs-PH also shows a tendency to transfer electrons to PMS, which implies that the PH modification improves the ability of o-CQDs to donate electron to and activate PMS, consequently enhancing the photooxidation efficiency. Moreover, the photogenerated electrons were preferentially transferred to the adsorbed PMS via the PH group, which helps to bind with PMS and deliver the electron for PMS decomposition into superoxide radicals.

Based on these results, a possible mechanism for CQD-based photocatalytic activation of PMS and degradation of pollutants was proposed in Fig. 12. o-CQDs-PH was excited and generated photogenerated electrons and holes under visible light irradiation. The PMS was preferentially adsorbed onto the PH group on the o-CQDs-PH surface and was then further activated by electrons in the electron-rich region of the C═N-N bond to generate $O_2^{\bullet-}$ during the o-CQDs-PH/PMS process. Finally, TC was attacked by h^+ and $O_2^{\bullet-}$ and degraded into smaller harmless byproducts. Based on the above analysis, a generation route of h^+ and $O_2^{\bullet-}$ has been proposed as Eqs. (1–4).

$$o-CQDs-PH + h\nu \rightarrow h^+ + e^- \quad (1)$$

$$HSO_5^- + e^- \rightarrow HO_2^{\cdot} + SO_3^{2-} \quad (2)$$

$$HO_2^{\cdot} \rightarrow H^+ + O_2^{\cdot-} \quad (3)$$

$$h^+/O_2^{\cdot-} + \text{pollutants} \rightarrow \text{Products} \quad (4)$$

4. Conclusion

In this study, we prepared CQDs with different oxygen contents by controlling the carbonation temperature, where $CQDs_{200}$ was

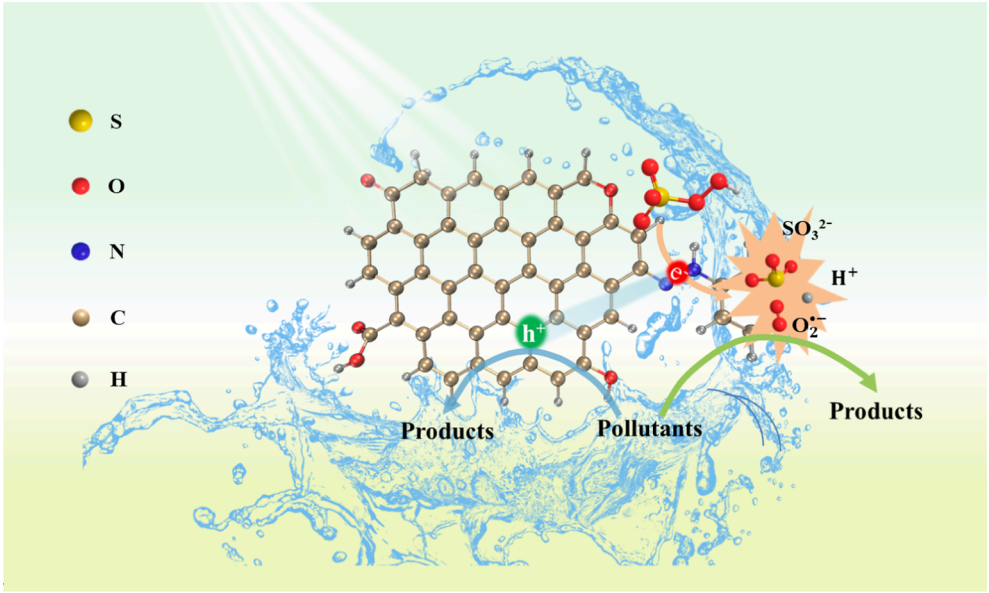

Fig. 12. PMS activation mechanism over o-CQDs-PH catalyst.

determined to have the best PMS activation performance with TC removal rate of 51.5% in 60 min. Through selective chemical titration of C-OH, COOH and C═O groups, the C═O species was identified as the most dominant active site for PMS activation. The removal of TC by o-CQDs was improved to 67.4% within 60 min when the C-OH is oxidized to a C═O group using DMP. Alternatively, and mmonia and phenylhydrazine were used to modify the carbon dots through oriented chemical reactions with specific oxygen-containing functional groups. Our experimental and theoretical results show that ammonia treatment selectively removed carboxyl and epoxide groups and introduced amino groups to reduce the non-radiative recombination centers (oxygen groups), thereby promoting the complexation of photogenerated electron-hole pairs and leading to poor photocatalytic activity. The introduction of pH to the surface of o-CQDs can effectively regulate the electronic structure to facilitate PMS adsorption, electron transfer, and surface redox reaction. The photogenerated electrons are then preferentially transferred to the adsorbed PMS through the PH group to generate $O_2^{\bullet-}$, which collaborates with photogenerated holes to degrade organic pollutants in water. The findings will provide advanced protocols for developing highly efficient metal-free photocatalysts for persulfate-based advanced oxidation processes.

CRediT authorship contribution statement

Wenyuan Han: Conceptualization, Investigation, Formal analysis, Writing – original draft. **Degang Li:** Investigation, Validation, Writing – original draft. **Yifan Kong:** Formal analysis, Investigation. **Wei Liu:** Validation, Formal analysis. **Wenwu Qin:** Visualization, Conceptualization, Supervision, Writing – review & editing, Project administration. **Shaobin Wang:** Conceptualization, Writing – review & editing. **Xiaoguang Duan:** Conceptualization, Methodology, Writing – review & editing, Supervision.

Declaration of Competing Interest

The authors declare that they have no known competing financial interests or personal relationships that could have appeared to influence the work reported in this paper.

Data availability

Data will be made available on request.

Acknowledgement

The author acknowledge the financial support from Australian Research Council (ARC-DE210100253) and National Computational Infrastructure (NCMAS-2023-78).

Appendix A. Supplementary data

Supplementary data to this article can be found online at https://doi.org/10.1016/j.jcis.2023.05.092.

References

[1] C. Long, Z. Jiang, J. Shangguan, T. Qing, P. Zhang, B. Feng, Applications of carbon dots in environmental pollution control: A review, Chem. Eng. J. 406 (2021), 126848.
[2] N. Yadav, V.K. Garg, A.K. Chhillar, J.S. Rana, Detection and remediation of pollutants to maintain ecosustainability employing nanotechnology: A review, Chemosphere 280 (2021), 130792.
[3] B.T. Zhang, X. Zheng, H.F. Li, J.M. Lin, Application of carbon-based nanomaterials in sample preparation: A review, Anal. Chim. Acta 784 (2013) 1–17.
[4] J. Liu, R. Li, B. Yang, Carbon dots: A new type of carbon-based nanomaterial with wide applications, ACS Cent. Sci. 6 (12) (2020) 2179–2195.
[5] M.E. Khan, A. Mohammad, T. Yoon, State-of-the-art developments in carbon quantum dots (CQDs): Photo-catalysis, bio-imaging, and bio-sensing applications, Chemosphere 302 (2022), 134815.
[6] M.J. Molaei, A review on nanostructured carbon quantum dots and their applications in biotechnology, sensors, and chemiluminescence, Talanta 196 (2019) 456–478.
[7] S. Hu, Q. Chang, K. Lin, J. Yang, Tailoring surface charge distribution of carbon dots through heteroatoms for enhanced visible-light photocatalytic activity, Carbon 105 (2016) 484–489.
[8] D.L. Zhao, T.S. Chung, Applications of carbon quantum dots (CQDs) in membrane technologies: A review, Water Res. 147 (2018) 43–49.
[9] M. Pan, X. Xie, K. Liu, J. Yang, L. Hong, S. Wang, Fluorescent carbon quantum dots-synthesis, functionalization and sensing application in food analysis, Nanomaterials 10 (2020) 930.
[10] V. Manikandan, N.Y. Lee, Green synthesis of carbon quantum dots and their environmental applications, Environ. Res. 212 (2022), 113283.
[11] T.J. Pillar-Little, N. Wanninayake, L. Nease, D.K. Heidary, E.C. Glazer, D.Y. Kim, Superior photodynamic effect of carbon quantum dots through both type I and type II pathways: Detailed comparison study of top-down-synthesized and bottom-up-synthesized carbon quantum dots, Carbon 140 (2018) 616–623.
[12] A. Yadegari, J. Khezri, S. Esfandiari, H. Mahdavi, A.A. Karkhane, R. Rahighi, R. Heidarimoghadam, L. Tayebi, E. Hashemi, A. Farmany, Bottom-up synthesis of nitrogen and oxygen co-decorated carbon quantum dots with enhanced DNA plasmid expression, Colloid. Surface. B. 184 (2019), 110543.
[13] S. Zhu, Y. Song, X. Zhao, J. Shao, J. Zhang, B. Yang, The photoluminescence mechanism in carbon dots (graphene quantum dots, carbon nanodots, and polymer dots): current state and future perspective, Nano Res. 8 (2015) 355–381.
[14] S. Hu, Y. Ding, Q. Chang, J. Yang, K. Lin, Chlorine-functionalized carbon dots for highly efficient photodegradation of pollutants under visible-light irradiation, Appl. Surf. Sci. 355 (2015) 774–777.
[15] N.A. Travlou, D.A. Giannakoudakis, M. Algarra, A.M. Labella, E. Rodríguez-Castellón, T.J. Bandosz, S-and N-doped carbon quantum dots: Surface chemistry dependent antibacterial activity, Carbon 135 (2018) 104–111.
[16] Z. Zhang, J.T. Yates Jr, Band bending in semiconductors: chemical and physical consequences at surfaces and interfaces, Chem. Rev. 112 (2012) 5520–5551.
[17] H. Li, Z. Zheng, M. Liu, H. Jiang, D. Hu, X. Zhang, L. Xia, X. Geng, J. Lu, X. Cheng, Visible light photo-treatment of simulated wastewater activated by high-efficient photocatalyst: A novel heterojunction of Bi_2MoO_6 balls and Pd nanoskeletons, Appl. Surf. Sci. 510 (2020), 145468.
[18] Y. Hong, Y. Meng, G. Zhang, B. Yin, Y. Zhao, W. Shi, C. Li, Facile fabrication of stable metal-free CQDs/g-C_3N_4 heterojunctions with efficiently enhanced visible-light photocatalytic activity, Sep. Purif. Technol. 171 (2016) 229–237.
[19] N. Shao, Z. Hou, H. Zhu, J. Wang, C.P. François-Xavier, Novel 3D core-shell structured CQDs/Ag_3PO_4@ Benzoxazine tetrapods for enhancement of visible-light photocatalytic activity and anti-photocorrosion, Appl. Catal. B: Environ. 232 (2018) 574–586.
[20] X. Yu, J. Liu, Y. Yu, S. Zuo, B. Li, Preparation and visible light photocatalytic activity of carbon quantum dots/TiO_2 nanosheet composites, Carbon 68 (2014) 718–724.
[21] Q. Lu, Y. Zhang, S. Liu, Graphene quantum dots enhanced photocatalytic activity of zinc porphyrin toward the degradation of methylene blue under visible-light irradiation, J. Mater. Chem. A. 3 (2015) 8552–8558.
[22] Y. Yao, H. Zhang, K. Hu, G. Nie, Y. Yang, Y. Wang, X. Duan, S. Wang, Carbon dots based photocatalysis for environmental applications, J. Environ. Chem. Eng. 10 (2022), 107336.
[23] M. Ali, A.S. Anjum, R. Riaz, A. Bibi, K.C. Sun, S.H. Jeong, Unraveling the surface states related Stokes shift dependent electrocatalytic activity of N-doped carbon quantum dots for photovoltaic applications, Carbon 181 (2021) 155–168.
[24] L. Han, S.G. Liu, J.X. Dong, J.Y. Liang, L.J. Li, N.B. Li, H.Q. Luo, Facile synthesis of multicolor photoluminescent polymer carbon dots with surface-state energy gap-controlled emission, J. Mater. Chem. C. 5 (2017) 10785–10793.
[25] T. Lu, F. Chen, Multiwfn: A multifunctional wavefunction analyzer, J. Comput. Chem. 33 (2012) 580–592.
[26] Z. Liu, T. Lu, Q. Chen, An sp-hybridized all-carboatomic ring, cyclo[18] carbon: Electronic structure, electronic spectrum, and optical nonlinearity, Carbon 165 (2020) 461–467.
[27] S. Chen, T. Luo, K. Chen, Y. Lin, J. Fu, K. Liu, C. Cai, Q. Wang, H. Li, X. Li, Chemical identification of catalytically active sites on oxygen-doped carbon nanosheet to decipher the high activity for electr-synthesis hydrogen peroxide, Angew. Chem. Int. Edit. 133 (2021) 16743–16750.
[28] D. Li, X. Duan, H. Sun, J. Kang, H. Zhang, M.O. Tade, S. Wang, Facile synthesis of nitrogen-doped graphene via low-temperature pyrolysis: the effects of precursors and annealing ambience on metal-free catalytic oxidation, Carbon 115 (2017) 649–658.
[29] T. Okpalugo, P. Papakonstantinou, H. Murphy, J. McLaughlin, N. Brown, High resolution XPS characterization of chemical functionalised MWCNTs and SWCNTs, Carbon 43 (2005) 153–161.
[30] W. Ren, L. Xiong, G. Nie, H. Zhang, X. Duan, S. Wang, Insights into the electron-transfer regime of peroxydisulfate activation on carbon nanotubes: the role of oxygen functional groups, Environ. Sci. Technol. 54 (2019) 1267–1275.
[31] W. Han, D. Li, M. Zhang, H. Ximin, X. Duan, S. Liu, S. Wang, Photocatalytic activation of peroxymonosulfate by surface-tailored carbon quantum dots, J. Hazard. Mater. 395 (2020), 122695.
[32] X. Tang, H. Yu, B. Bui, L. Wang, C. Xing, S. Wang, M. Chen, Z. Hu, W. Chen, Nitrogen-doped fluorescence carbon dots as multi-mechanism detection for iodide and curcumin in biological and food samples, Bioact. Mater. 6 (2021) 1541–1554.
[33] H. Ding, S.B. Yu, J.S. Wei, H.M. Xiong, Full-color light-emitting carbon dots with a surface-state-controlled luminescence mechanism, ACS, Nano. 10 (2016) 484–491.

[34] C. Zhang, D. Qin, Y. Zhou, F. Qin, H. Wang, W. Wang, Y. Yang, G. Zeng, Dual optimization approach to Mo single atom dispersed g-C_3N_4 photocatalyst: Morphology and defect evolution, Appl. Catal. B: Environ. 303 (2022), 120904.
[35] X. Cheng, H. Guo, Y. Zhang, X. Wu, Y. Liu, Non-photochemical production of singlet oxygen via activation of persulfate by carbon nanotubes, Water Res. 113 (2017) 80–88.
[36] E.-T. Yun, H.-Y. Yoo, H. Bae, H.I. Kim, J. Lee, Exploring the role of persulfate in the activation process: radical precursor versus electron acceptor, Environ. Sci. Technol. 51 (2017) 10090–10099.
[37] H. Sun, A. Zhao, N. Gao, K. Li, J. Ren, X. Qu, Deciphering a nanocarbon-based artificial peroxidase: chemical identification of the catalytically active and substrate-binding sites on graphene quantum dots, Angew. Chem. Int. Edit. 54 (2015) 7176–7180.
[38] W. Qi, W. Liu, B. Zhang, X. Gu, X. Guo, D. Su, Oxidative dehydrogenation on nanocarbon: identification and quantification of active sites by chemical titration, Angew. Chem. Int. Edit. 52 (2013) 14224–14228.
[39] H. Zheng, Q. Wang, Y. Long, H. Zhang, X. Huang, R. Zhu, Enhancing the luminescence of carbon dots with a reduction pathway, Chem. Commun. 47 (2011) 10650–10652.
[40] B. Cao, H. Park, M.M. Joullié, Total synthesis of ustiloxin D, J. Am. Chem. Soc. 124 (2002) 520–521.
[41] D.B. Dess, J. Martin, A useful 12-I-5 triacetoxyperiodinane (the Dess-Martin periodinane) for the selective oxidation of primary or secondary alcohols and a variety of related 12-I-5 species, J. Am. Chem. Soc. 113 (1991) 7277–7287.
[42] J.M.D. Dikdim, Y. Gong, G.B. Noumi, J.M. Sieliechi, X. Zhao, N. Ma, M. Yang, J. B. Tchatchueng, Peroxymonosulfate improved photocatalytic degradation of atrazine by activated carbon/graphitic carbon nitride composite under visible light irradiation, Chemosphere 217 (2019) 833–842.
[43] B. Li, H. Song, F. Han, L. Wei, Photocatalytic oxidative desulfurization and denitrogenation for fuels in ambient air over Ti_3C_2/g-C_3N_4 composites under visible light irradiation, Appl. Catal. B: Environ. 269 (2020), 118845.
[44] J. Xu, S. Sahu, L. Cao, P. Anilkumar, K.N. Tackett, H. Qian, C.E. Bunker, E. A. Guliants, A. Parenzan, Y.P. Sun, Carbon nanoparticles as chromophores for photon harvesting and photoconversion, ChemPhysChem 12 (2011) 3604–3608.
[45] Y. Zhou, H. Sun, F. Wang, J. Ren, X. Qu, How functional groups influence the ROS generation and cytotoxicity of graphene quantum dots, Chem. Commun. 53 (2017) 10588–10591.
[46] R. Tian, S. Hu, L. Wu, Q. Chang, J. Yang, J. Liu, Tailoring surface groups of carbon quantum dots to improve photoluminescence behaviors, Appl. Surf. Sci. 301 (2014) 156–160.
[47] H. Ming, P. Zhang, Y. Yang, Y. Zou, C. Yang, Y. Hou, K. Ding, J. Zhang, X. Wang, Tailored poly-heptazine units in carbon nitride for activating peroxymonosulfate to degrade organic contaminants with visible light, Appl. Catal. B: Environ. 311 (2022), 121341.
[48] X. Duan, W. Li, Z. Ao, J. Kang, W. Tian, H. Zhang, S.-H. Ho, H. Sun, S. Wang, Origins of boron catalysis in peroxymonosulfate activation and advanced oxidation, J. Mater. Chem. A. 7 (2019) 23904–23913.
[49] X. Duan, Z. Ao, H. Sun, L. Zhou, G. Wang, S. Wang, Insights into N-doping in single-walled carbon nanotubes for enhanced activation of superoxides: a mechanistic study, Chem. Commun. 51 (2015) 15249–15252.
[50] H. Lee, H.J. Lee, J. Jeong, J. Lee, N.-B. Park, C. Lee, Activation of persulfates by carbon nanotubes: oxidation of organic compounds by nonradical mechanism, Chem. Eng. J. 266 (2015) 28–33.
[51] H. Zhang, C. Xie, L. Chen, J. Duan, F. Li, W. Liu, Different reaction mechanisms of $SO4^{\bullet-}$ and •OH with organic compound interpreted at molecular orbital level in Co (II)/peroxymonosulfate catalytic activation system, Water Res. 229 (2023), 119392.
[52] S. Liu, Q. Pan, J. Li, M. Wang, J. Zhang, Y. Song, C. Zhao, J. Shi, H. Deng, Enhanced mediated electron transfer pathway of peroxymonosulfate activation dominated with graphitic-N for the efficient degradation of various organic contaminants in multiple solutions, ACS EST Water. 2 (2022) 817–829.
[53] H. Wang, W. Guo, Q. Si, B. Liu, Q. Zhao, H. Luo, N. Ren, Non-covalent doping of carbon nitride with biochar: Boosted peroxymonosulfate activation performance and unexpected singlet oxygen evolution mechanism, Chem. Eng. J. 418 (2021), 129504.
[54] X. Chen, X. Duan, W.D. Oh, P.H. Zhang, C.T. Guan, Y.A. Zhu, T.-T. Lim, Insights into nitrogen and boron-co-doped graphene toward high-performance peroxymonosulfate activation: Maneuverable NB bonding configurations and oxidation pathways, Appl. Catal. B: Environ. 253 (2019) 419–432.
[55] T. Le Bahers, C. Adamo, I. Ciofini, A qualitative index of spatial extent in charge-transfer excitations, J. Chem. Theory Comput. 7 (2011) 2498–2506.